

A WIDE AREA SURVEY FOR HIGH-REDSHIFT MASSIVE GALAXIES. II. NEAR-INFRARED SPECTROSCOPY OF BzK-SELECTED MASSIVE STAR-FORMING GALAXIES¹

MASATO ONODERA^{2,3}, NOBUO ARIMOTO^{4,5}, EMANUELE DADDI², ALVIO RENZINI⁶, XU KONG⁷, ANDREA CIMATTI⁸, TOM BROADHURST⁹, AND DAVE M. ALEXANDER¹⁰

Accepted for publication in Astrophysical Journal

ABSTRACT

Results are presented from near-infrared spectroscopic observations of a sample of BzK-selected, massive star-forming galaxies (*sBzKs*) at $1.5 < z < 2.3$ that were obtained with OHS/CISCO at the Subaru telescope and with SINFONI at the VLT. Among the 28 *sBzKs* observed, H α emission was detected in 14 objects, and for 11 of them the [N II] λ 6583 flux was also measured. Multiwavelength photometry was also used to derive stellar masses and extinction parameters, whereas H α and [N II] emissions have allowed us to estimate star-formation rates (SFR), metallicities, ionization mechanisms, and dynamical masses. In order to enforce agreement between SFRs from H α with those derived from rest-frame UV and mid-infrared, additional obscuration from the emission lines (that originate in H II regions) was required compared to the extinction derived from the slope of the UV continuum. We have also derived the stellar mass-metallicity relation, as well as the relation between stellar mass and specific SFR, and compared them to the results in other studies. At a given stellar mass, the *sBzKs* appear to have been already enriched to metallicities close to those of local star-forming galaxies of similar mass. The *sBzKs* presented here tend to have higher metallicities compared to those of UV-selected galaxies, indicating that near-infrared selected galaxies tend to be a chemically more evolved population. The *sBzKs* show specific SFRs that are systematically higher, by up to ~ 2 orders of magnitude, compared to those of local galaxies of the same mass. The empirical correlations between stellar mass and metallicity, and stellar mass and specific SFR are then compared with those of evolutionary population synthesis models constructed either with the simple closed-box assumption, or within an infall scenario. Within the assumptions that are built-in such models, it appears that a short timescale for the star-formation ($\simeq 100$ Myr) and large initial gas mass appear to be required if one wants to reproduce both relations simultaneously.

Subject headings: galaxies: star-formation — galaxies: evolution — galaxies: metallicity — galaxies: high-redshift

1. INTRODUCTION

Much action takes place during the ~ 2 billion years of cosmic time between $z = 3$ and $z = 1.4$: both the global star-formation rate (SFR) and nuclear (AGN) activity peak at $z \sim 2$, while much of the galaxy assembly and morphological differentiation are taking place and a population of massive, passively evolving galaxies is gradually emerging. Thus a full exploration of this redshift interval is critical for our understanding of galaxy evolution. Unfortunately, this is also a relatively difficult redshift range to penetrate observationally,

as strong spectral features such as Ca II H&K and the 4000 Å break (for passive galaxies) and [O II] λ 3727, [O III] λ 5007, H α and H β (for star forming ones) have all moved to the near-infrared (NIR).

Still, most spectroscopic surveys of galaxies at $1.4 \lesssim z \lesssim 3$ have used optical spectrographs, relying on much weaker spectroscopic features for redshift determination and galaxy characterization, with these limitations being partly compensated by the possibility to achieve a fairly high multiplex (e.g., Steidel et al. 2004; Mignoli et al. 2005; Le Fèvre et al. 2005; Vanzella et al. 2005; Lilly et al. 2007; Cimatti et al. 2008; Popesso et al. 2009). For passive galaxies at $z > 1.4$ such features practically restrict to a set of absorption features at $\lambda \sim 2600\text{--}2850$ Å due to neutral and singly ionized Mg and Fe, and for star-forming galaxies to several weak absorption lines over the rest-frame UV continuum, most of which due to the interstellar medium (ISM) of these galaxies.

The intrinsic weakness of the absorptions and/or of the continuum made such spectroscopic observations very demanding in terms of telescope time. Therefore, several studies of large samples of galaxies at $1.4 \lesssim z \lesssim 2.5$ have relied on color selections and photometric redshifts. Particularly effective has proven the BzK criterion introduced by Daddi et al. (2004a), which is able to select both star-forming (called *sBzKs*) as well as passively evolving galaxies (*pBzKs*) over this redshift range. This has enabled estimates of SFRs, stellar masses, and clustering properties of such galaxies, with samples from ~ 100 's to over $\sim 30,000$ objects (e.g., Kong et al. 2006; Daddi et al. 2007a; Dunne et al.

¹ Based on data collected at Subaru Telescope, which is operated by the National Astronomical Observatory of Japan (S04A-081, S05A-098), and on observations collected at the European Southern Observatory, Paranal, Chile (075.A-0439).

² CEA, Laboratoire AIM-CNRS-Université Paris Diderot, Irfu/SAP, Orme des Merisiers, F-91191 Gif-sur-Yvette, France; masato.onodera@cea.fr

³ Department of Astronomy, Yonsei University, Sinchon-dong 134, Seodaemun-gu, Seoul, South Korea

⁴ National Astronomical Observatory of Japan, Osawa 2-21-1, Mitaka, Tokyo, Japan

⁵ Graduate University for Advanced Studies, Osawa 2-21-1, Mitaka, Tokyo, Japan

⁶ INAF-Padova, Vicolo dell'Osservatorio 5, I-35122 Padova, Italy

⁷ CfA, University of Science and Technology of China, Hefei 230026, China

⁸ Dipartimento di Astronomia, Università di Bologna, Via Ranzani 1, 40127 Bologna, Italy

⁹ School of Physics and Astronomy, Tel Aviv University, Tel Aviv 69978, Israel

¹⁰ Institute for Computational Cosmology, Department of Physics, Durham University, Durham DH1 3LE, UK

2009; McCracken et al. 2010). The BzK technique ensures a nearly unbiased selection of $z \sim 2$ galaxies, including UV-selected galaxies and single color, NIR-selected galaxies (e.g., Reddy et al. 2005; McCracken et al. 2010).

Whereas many aspects concerning the evolution of galaxies can be investigated using only photometric redshifts, spectroscopy remains indispensable for a variety of investigations. These include full mapping of the local environment (locating clusters, groups, filaments and voids), refining SFR and mass estimates, measure stellar and ISM metallicities, and finally map the internal dynamical workings of galaxies via 3D spectroscopy. In this respect, the required telescope time is not the only drawback of the optical spectroscopy of galaxies at $1.4 \lesssim z \lesssim 3$. Indeed, optical spectroscopy down to a limit as faint as $B \sim 25$ does not recover but a minor fraction of the global SFR and stellar mass at $z \sim 2$, in particular missing galaxies that are among the most massive and most intensively star-forming ones (Renzini & Daddi 2009). Moreover, high spatial resolution, 3D spectroscopy of high redshift galaxies requires the knowledge of the spectroscopic redshift, to make sure that interesting emission lines (e.g., $H\alpha$) are free from OH and other atmospheric contaminations (see e.g., Genzel et al. 2006; Förster Schreiber et al. 2009).

In the case of star-forming ($sBzK$) galaxies, the poor correlation of mass and SFR with B magnitude is a result of high extinction. Therefore, the situation should appear more favorable in the NIR, and not only because moving to longer wavelengths should reduce the impact of extinction, but also because the most active star-forming and most massive galaxies are also among the brightest objects at these longer wavelengths, and one can access strong emission lines such as [O II] and $H\alpha$. Yet, NIR spectroscopy of $z \gtrsim 1.4$ galaxies is still in its infancy, especially for NIR selected samples. Erb et al. (2006a,b,c) have presented results for over 100 UV-selected galaxies at $z \sim 2$, deriving SFRs from the strength of $H\alpha$. NIR spectroscopic observations of samples of $z \sim 2$ galaxies selected in the NIR have been also presented by Kriek et al. (2006a,b, 2007, 2008a,b), focusing mainly (but not exclusively) on passive galaxies by detecting the 4000 Å break, and deriving spectro-photometric redshifts from it. NIR spectroscopy of $sBzK$ galaxies has been carried out by Hayashi et al. (2009) for a sample of 40 $sBzK$ s, and detected $H\alpha$ emission from 15 of them. Their detections, however, are limited to $z < 2$. Finally, integral field NIR spectroscopy for some 60 star forming galaxies at $z \sim 2$ has been obtained by Förster Schreiber et al. (2009), for partly UV-selected, partly BzK -selected targets. Therefore, there is still just scanty spectroscopic information in the rest-frame optical wavelength for actively star-forming and heavily obscured galaxies at $z \simeq 2$, many of which would be missed by the UV-selection, and are virtually unreachable by current optical spectroscopy.

In the perspective of improving upon this situation, in 2004 we started NIR spectroscopic observations of $z \sim 2$ galaxies primarily selected on BzK technique, and using a variety of NIR instruments, namely OHS, CISCO and MOIRCS, at the Subaru telescope and SINFONI at the VLT. Our intent was to explore the effectiveness of NIR spectroscopy to improve our characterization of $z \sim 2$ galaxies using a relatively small pilot sample of them, while assessing the feasibility of wider surveys with future instruments with higher multiplex. In this paper we present the results of observations with the OHS/CISCO instruments on Subaru and SINFONI instrument on VLT of $sBzK$ galaxies, leaving the re-

sults obtained with the MOIRCS instrument for a future paper. With the observations presented here we have attempted to measure for each galaxy the dust extinction, SFR, ISM metallicity, and dynamical mass, while checking for a possible AGN contribution. Physical quantities are derived assuming the concordance cosmology, i.e., $\Omega_M = 0.3$, $\Omega_\Lambda = 0.7$, and $H_0 = 70 \text{ km s}^{-1} \text{ Mpc}^{-1}$ and photometric magnitudes are expressed in the AB system (Oke & Gunn 1983) if it is not explicitly noted otherwise. For the solar oxygen abundance, we use $12 + \log(\text{O}/\text{H})_\odot = 8.69$ (Allende Prieto et al. 2001). Emission line width are measured assuming a Gaussian profile and the FWHM and the velocity dispersion (σ) is given by $\text{FWHM} = 2.355\sigma$.

2. SAMPLE SELECTION, OBSERVATIONS, AND DATA REDUCTION

2.1. Sample Selection

The $sBzK$ galaxies which are the object of the present study have been culled from the K -band selected catalog of objects in the EIS Deep3a field and Daddi field, which are described along with the photometric data in Kong et al. (2006, hereafter K06). We have primarily selected $sBzK$ s with spectroscopically confirmed redshifts from the rest-frame UV spectroscopy obtained with the VIMOS instrument at the VLT (Daddi et al., in preparation). Then we have selected those for which the $H\alpha$ emission line falls at wavelengths where atmospheric and instrumental transmission are high and is not contaminated by OH-airglow lines. Additional criteria have then been applied to select objects which (1) are bright in the K -band ($K_{AB} \lesssim 22$) to select massive galaxies, i.e., $M_* \gtrsim 5 \times 10^{10} M_\odot$ (Daddi et al. 2004a, see also §4.1), (2) have red $z-K$ colors, $(z-K)_{AB} \gtrsim 2$ to select possibly more reddened ones, (3) are not detected in X-rays down to $(2-7) \times 10^{-16} \text{ ergs s}^{-1} \text{ cm}^{-2}$ (if in the Daddi field) and do not show strong AGN features in rest-frame UV spectra, so to exclude galaxies with an obvious AGN contribution, and (4) are bright in *Spitzer*/MIPS 24 μm images, with flux $\gtrsim 70 \mu\text{Jy}$ (for the Daddi field) and $\gtrsim 100 \mu\text{Jy}$ (for the Deep3a field), to make sure that they are actively forming stars.

Our selected objects in the Daddi field are not detected in *XMM-Newton*/*Chandra* X-ray data with 0.5–2 keV luminosities $L_X \lesssim 10^{43} \text{ ergs s}^{-1}$, which ensures the exclusion of luminous unobscured AGNs (M. Brusa, private communications). However, one $sBzK$ in our sample shows mid-IR (MIR) excess which suggests it may host an obscured AGN (see §5.3; Daddi et al. 2007a,b). We note that only 10 of our 28 objects comply to all the above constraints, and pairs of $sBzK$ s that can be put in the same slit have been preferentially included to have a larger sample. Among the 28 objects selected for NIR spectroscopy, 20 objects have a redshift from rest-frame UV spectra, and 13 objects satisfy all 4 criteria above and have a spectroscopic redshift. Object IDs, coordinates, redshifts from rest-frame UV spectra, and magnitudes are listed in Table 1.

2.2. OHS/CISCO Spectra

Among the selected objects, 7 $sBzK$ s were observed on May 1, 2004 and April 24–26, 2005, by using the OH-airglow suppressor (OHS; Iwamuro et al. 2001) with the Cooled Infrared Camera and Spectrograph for OHS (CISCO; Motohara et al. 2002) mounted on the Nasmyth focus on the Subaru telescope. The *JH* grism covering the 1.1–1.8 μm spectral range and a 1" slit were used, which give a spectral resolution

$R \simeq 200$. On May 6, 2004 and April 30, 2005 K -band spectroscopy with the wK grism covering the $1.85\text{--}2.5\mu\text{m}$ spectral range was carried out for 5 *sBzKs* with CISCO (i.e., without OHS), which with a slit width of $1''$ gives a resolution $R \simeq 300$. Position angles were selected to put bright nearby objects into the slit, so to facilitate target acquisition since our targets are usually too faint to be seen on acquisition images. In case no nearby object was available, target acquisition was made with blind offset from bright objects as close as possible to the target object. Each spectrum was obtained by taking $4 \times (900\text{s or }1000\text{s})$ exposure sequences with slightly modified ABBA standard nodding pattern to avoid bad pixels. As spectroscopic standards to correct for atmospheric and instrumental transmission, the A-type stars SAO 120721, SAO 121153, SAO 122123, SAO 180911, and SAO 180521 were observed for the *JH* grism, while the white dwarf GD 153 and the A-type star SAO 121856 were observed for the wK grism.

All the data were reduced with standard procedures. Two dimensional spectra were produced with flat fielding, distortion correction, bad pixel rejection, and sky subtraction by making a median sky from adjacent detector areas. Sky residuals were subtracted by fitting polynomials in the spatial direction, and then co-addition was carried out with appropriate offsets for the dithering width. The resulting 2D spectra were then collapsed to 1D spectra. The tilt of the spectra on the array was corrected by adopting the tilt of standard star spectra. The wavelength calibrations were carried out by using the standard pixel-wavelength relation of OHS/CISCO with systematic error of < 0.5 pixels (3\AA and 5\AA for OHS and CISCO, respectively; Motohara et al. 2001). Atmospheric and instrumental transmissions were corrected by using the 1D spectra of the standard stars reduced in the same way as object frames.

The absolute flux calibrations were carried out by comparing the photometric J - and K -band fluxes with those derived from the object spectra convolved with the filter transmission curves. Here we have adopted $2''$ aperture magnitudes, hence assuming that in the observed spectra both continuum and lines come from same region of a galaxy. Noise spectra were derived by measuring rms of counts in the blank sky region.

2.3. SINFONI Spectra

On April 14–16, 2005 we observed 16 *sBzKs* with the Spectrograph for Integral Field Observations in the Near Infrared (SINFONI; Eisenhauer et al. 2003; Bonnet et al. 2004) at the VLT/UT4. The $H+K$ grating covering the $1.45\text{--}2.45\mu\text{m}$ spectral range with $R \simeq 1500$ and a pre-optics giving a 125×250 mas pix^{-1} spatial resolution were used. Each object was observed by 1 or 2 sequence(s) of $4 \times (450\text{s or }900\text{s})$ exposures with 4 arcsec dithering both in x - and y -direction. The B-type stars, HIP 007873, HIP 026816, HIP 031768, HIP 068100, HIP 068372, HIP 072367, HIP 075711, HIP 083861, HIP 092957, HIP 094333, HIP 095806, and HIP 099244, were observed as spectroscopic standards.

The reductions of SINFONI data were carried out with the SINFONI pipeline¹¹ and custom scripts, including flat-fielding, sky-subtraction by median sky of a sequence, bad pixel rejection, distortion correction, wavelength calibration by arc lamp frames, cube reconstruction, residual sky subtraction by subtracting the median in x -direction from each pixels, and finally co-addition with appropriate offsets. Telluric and instrumental absorptions were corrected with spectroscopic

standard star frames. Since neither the standard stars nor the objects are affected by slit losses, the absolute flux calibrations were obtained by dividing the object spectrum by the standard star spectrum, scaled to the broad band photometric magnitudes.

3. EMISSION LINE MEASUREMENTS

Among the 28 *sBzKs* observed, emission lines were detected in 13 of them, and identified as $H\alpha$ in all cases. Emission lines in the SINFONI data cube have also been detected in an object in the vicinity of Dad-2426 (hence named Dad-2426b), and the lines are identified as $H\alpha$ and $[\text{N II}]\lambda 6583$ at $z = 1.772$ according to the separation between them. Optical composite images and K -band images of the galaxies with $H\alpha$ detections are shown in Figure 1, and their spectra around $H\alpha$ are shown in Figures 2 and 3 for OHS/CISCO and SINFONI, respectively.

Due to their low resolution in wavelength, the $H\alpha$ emission is always blended with $[\text{N II}]\lambda\lambda 6548, 6583$ in the OHS/CISCO spectra, while these lines are resolved in the SINFONI spectra. We have measured the $H\alpha$ line fluxes by fitting multiple-Gaussians for $H\alpha$ and $[\text{N II}]\lambda\lambda 6548, 6583$, assuming that all three lines have same width, $[\text{N II}]\lambda 6583/[\text{N II}]\lambda 6548 = 3$, and a constant continuum flux. This leaves redshift, $H\alpha$ emission line flux $f(H\alpha)$, flux ratio $f(H\alpha)/f([\text{N II}]\lambda 6583)$, line width σ , and constant continuum flux as free parameters. For most of the objects, the fitting converged to a single solution against various initial guesses, and the derived line widths agree with those expected from instrumental resolution in the case of OHS/CISCO spectra. However, there are several exceptions. For D3a-8608 and Dad-2426 the procedure did not converge to stable solutions, and we fixed the line width to that of the instrumental profile (measured on the OH lines close to the position of emission lines). Small perturbations to the assumed line widths did not change fluxes and equivalent widths (EWs) appreciably. Since the $[\text{N II}]\lambda 6583$ line is below the detection limit in D3a-3287 and D3a-4626, only a single Gaussian to the $H\alpha$ line was fitted. D3a-11391 appears to have both broad and narrow $H\alpha$ components. This object also shows MIR-excess (Daddi et al. 2007b) as discussed later (§5.3), hence the spectrum was fitted with both broad and narrow $H\alpha$ lines, which resulted in a better χ^2 compared to the fit with only narrow line components. We could not find a good fit when including the $[\text{N II}]\lambda$ lines, possibly due to residual of OH sky lines and rapidly variable atmospheric transmission at the edge of H -band. The best fit Gaussian functions are overplotted in Figure 2 and 3.

The resulting redshifts derived from $H\alpha$, along with the fluxes and EWs of $H\alpha$ and $[\text{N II}]\lambda 6583$, and velocity dispersions are listed in Table 3. The EWs listed in Table 3 are derived with the measured line fluxes and continuum fluxes from the best-fit spectral energy distribution (SED) (see §4.1). $H\alpha$ EWs are also corrected for stellar $H\alpha$ absorption, derived from the synthetic spectrum that best-fits the SED. The error in the continuum flux from the best-fit SED around the position of $H\alpha$ is estimated to be 20%. For Dad-2426b, which is not listed in our K -selected catalog, the continuum flux is calculated from its 5σ limit of $K_{\text{AB}} = 21.5$, and the stellar $H\alpha$ EW is assumed to be 4.4\AA , which is the average of stellar $H\alpha$ EWs estimated for the other objects. These redshifts agree well with those from rest-frame UV spectra, except for 2 objects, Dad-2426 ($z_{\text{UV}} = 2.36$ and $z_{H\alpha} = 2.40$) and D3a-6397 ($z_{\text{UV}} = 2.00$ and $z_{H\alpha} = 1.51$). The spectrum of

¹¹ <http://www.eso.org/sci/data-processing/software/pipelines/>

Dad-2426 is located a little far from the detector center and since detector distortion increases with distance from the center, we first doubted that the adopted pixel-wavelength relation may not apply in such case. However, a cross-check of wavelength with OH lines showed that the wavelength was well calibrated. This object was also observed with SINFONI and a feature is marginally seen at $2.23\mu\text{m}$ which if due to $\text{H}\alpha$ corresponds to $z = 2.40$, consistent with the redshift from the CISCO spectrum. For D3a-6397, the discrepancy is very large, but its z_{UV} is quite uncertain whereas $[\text{N II}]\lambda 6583$ is well detected at the expected position relative to $\text{H}\alpha$, hence we consider $z_{\text{H}\alpha}$ as more reliable.

From the $\text{H}\alpha/[\text{N II}]\lambda 6583$ emission line ratio it is possible to estimate whether there is a significant contribution from an AGN component, though more emission lines such as $\text{H}\beta$ and $[\text{O III}]$ are required for a more robust diagnostic (e.g., Veilleux & Osterbrock 1987; Baldwin et al. 1981; Kauffmann et al. 2003). Here we classify *sBzKs* with $[\text{N II}]\lambda 6583/\text{H}\alpha < 0.7$ as star-formation dominated and those with $[\text{N II}]\lambda 6583/\text{H}\alpha > 0.7$ as AGN dominated (Swinbank et al. 2004). Adopting this criterion, one *sBzK*, D3a-8608, is classified as AGN-dominated. Besides the emission line ratio diagnostics, D3a-11391 could host an AGN because of its broad-line component. This would read an AGN fraction of $\simeq 15\%$ for our sample of 14 galaxies with detected emission lines. Note that true AGN fraction among *sBzKs* might be even higher, since part of the objects have been pre-selected for lacking AGN features. In any case, this AGN fraction is not far from that ($\simeq 25\%$) estimated for the full *sBzK* population in the Deep-3a and Daddi fields (K06), while up to $\simeq 50\%$ of massive ($M_* \simeq 10^{11} M_\odot$) *sBzKs* show MIR-excess, possibly related to heavily obscured AGN (Daddi et al. 2007b).

4. PHYSICAL PROPERTIES OF *sBzK* GALAXIES

4.1. Stellar Masses and Reddening

Stellar masses (M_*) and the reddening $E(B-V)$ were derived by SED fitting to the *BRIzJK*- and *BRiK*-band data for the *sBzKs* in the Deep3a field and the Daddi field, respectively. Spectroscopic redshifts determined from $\text{H}\alpha$ emission lines were used for the fit.

Template SEDs were generated by using PÉGASE.2 (Fioc & Rocca-Volmerange 1997, 1999), assuming a Salpeter initial mass function (IMF; Salpeter 1955) for stars with $0.1M_\odot$ to $120M_\odot$. These models assume exponentially declining SFRs and incorporate chemical evolution using chemical yields from Woosley & Weaver (1995). Real galaxies at $z \sim 2$ are unlikely to have evolved with exponentially declining SFRs (cf. Cimatti et al. 2008; Renzini 2009; Maraston et al. 2010), and their gas accretion histories may be radically different compared to those assumed in the PÉGASE.2 models. Although the use of these models introduces some rigidity in the SED fits, we believe that the derived stellar masses should be correct within a factor of ~ 2 (Drory et al. 2004). A systematic overestimate by up a factor ~ 3 may be present for those galaxies in which the bulk of stars have ages around ~ 1 Gyr, i.e., at the peak of the contribution by the TP-AGB phase of stellar evolution, that was not adequately included in the PÉGASE.2 (e.g., Maraston 1998, 2005; Kajisawa et al. 2009; Magdis et al. 2009). Furthermore, a systematic reduction by a factor $\sim 1.6-2$ of both SFRs and masses would be produced adopting a *bottom light* IMF, such as those of Kroupa (2002) or Chabrier (2003).

The adopted models assume SFR *e*-folding times from $\tau_{\text{sf}} = 100$ Myr to 500 Gyr with various age grids ranging from 10 Myr to 15 Gyr. The synthetic SEDs are then dust attenuated according to the Calzetti law (Calzetti 2001) with $0 < E(B-V) < 1.5$. Absorption by neutral hydrogen intervening along the line of sight is also applied (Madau 1995; Madau et al. 1996). Fitting is finally obtained by a χ^2 -minimization, with fixed redshift derived from $\text{H}\alpha$, and with the constraint that age cannot exceed the age of the universe at the observed redshift. Stellar masses are then derived by multiplying the luminosity by the M/L ratio of the model which best-fits the observed SED.

The best-fit SEDs together with observed data points are shown in Figure 4 and the derived stellar masses and reddenings are listed in Table 4. For a consistency check, the stellar masses and reddenings are also calculated by using the *BzK*-calibrations as given by Equation (4) and (6) in Daddi et al. (2004a):

$$E(B-V) = 0.25(B-z+0.1)_{\text{AB}}, \quad (1)$$

$$\log(M_*/10^{11} M_\odot) = -0.4(K_{\text{AB}}^{\text{tot}} - 21.38) + 0.218[(z-K)_{\text{AB}} - 2.29], \quad (2)$$

which are based on SED fits to the full *UBVRIZJHK*-band data (cf. *BRIzJK* in this study). These *BzK*-based stellar masses and reddening parameters are also reported in Table 1. Figure 5 shows the difference of stellar mass and reddening between the *BzK*-based values and those from SED fitting, for the $\text{H}\alpha$ detected objects, as a function of stellar masses from SED fitting. Average offsets and dispersion between two estimators are $\langle \log(M_{*\text{SED}}/M_{*\text{BzK}}) \rangle = 0.03$ and $\sigma(\log(M_{*\text{SED}}/M_{*\text{BzK}})) = 0.22$, respectively, for the stellar masses, and $\langle \Delta E(B-V) \rangle = -0.03$ and $\sigma(E(B-V)) = 0.07$, respectively, for the reddening. Hence, they agree reasonably well and without large systematic offsets.

4.2. $\text{H}\alpha$ Star-formation Rates

The $\text{H}\alpha$ luminosities are converted into SFRs following the relation in Kennicutt (1998):

$$\text{SFR}(M_\odot \text{yr}^{-1}) = 7.9 \times 10^{-42} L_{\text{H}\alpha} (\text{ergs s}^{-1}), \quad (3)$$

which assumes solar abundance, a Salpeter IMF, and constant SFR within the last 100 Myr. Although the conversion factor may vary from 2.6×10^{-42} to 8.7×10^{-42} , depending on metallicity, IMF, and star-formation history (Buat et al. 2002), we adopt Kennicutt's conversion as it is the most commonly used and it simplifies the comparison with results from the literature.

Although $\text{H}\alpha$ is usually considered to be relatively unaffected by dust extinction, dust extinction must be taken into account for galaxies like *sBzKs* which undergo vigorous star-formation and are likely to be heavily obscured by dust (Table 4; Daddi et al. 2005; Pannella et al. 2009). The $\text{H}\beta$ emission line would enable us to estimate the dust extinction via the Balmer decrement, but unfortunately it is not detected in our spectra. The 3σ upper limits for the $\text{H}\beta$ flux of $\text{H}\alpha$ detected *sBzKs* is $(\text{H}\alpha/\text{H}\beta)_{\text{limit}} > 2.86$, which cannot significantly constrain the reddening, except for D3a-4751 whose $\text{H}\alpha/\text{H}\beta > 5.0$ implies stellar $E(B-V) > 0.2$, consistent with the stellar $E(B-V) = 0.25$ from SED fitting. Correspondingly, the reddening values from SED fitting are used for the extinction correction of the $\text{H}\alpha$ luminosities. One

may expect that nebular emission lines from H II regions could suffer from larger dust extinction than the stellar continuum emission (Calzetti 2001). To cope with this problem, Cid Fernandes et al. (2005) compared the extinction of stellar continuum with that of nebular emission by using star-forming galaxies from the SDSS data set, and found a linear correlation between them. This relation was combined with the Calzetti extinction curve by Savaglio et al. (2005), obtaining:

$$A_V = 3.173 + 1.841A_V^* - 6.418 \log \left(\frac{H\alpha}{H\beta} \right)_{\text{th}}, \quad (4)$$

where A_V and A_V^* are gas and stellar visual extinctions, respectively, and $(H\alpha/H\beta)_{\text{th}}$ is the line flux ratio calculated from the atomic physics theory. Here we assumed the case B recombination with $T = 10000\text{K}$ and $(H\alpha/H\beta)_{\text{th}} = 2.86$ (Osterbrock & Ferland 2005). Extinction corrected $H\alpha$ SFRs are then derived by using A_V from the above relation. Visual extinctions of stars and gas, extinction at $H\alpha$, $H\alpha$ luminosities, and SFRs with and without extinction corrections are listed in Table 5.

After extinction correction, Dad-2426 and D3a-6397 show $\text{SFR} \gtrsim 1000M_{\odot}\text{yr}^{-1}$. Dad-2426 has been detected at 1.2 mm at more than 3σ level, and its SFR from FIR luminosity of $800\text{--}1900M_{\odot}\text{yr}^{-1}$ (Dannerbauer et al. 2006) is consistent with the $H\alpha$ -based SFR. In our sample with $H\alpha$ detection, more than half of the *sBzKs* have $\text{SFR} > 100M_{\odot}\text{yr}^{-1}$, after extinction correction. These $H\alpha$ SFRs $\gtrsim 100M_{\odot}\text{yr}^{-1}$ agree with the SFRs derived by the combination of UV and MIR for the *sBzKs* with similar range of stellar mass in GOODS fields (see §5.3; Daddi et al. 2005, 2007a). The comparison between SFRs from different indicators and different extinction corrections will be further discussed in §5.3.

4.3. Metallicities

Accurate metallicities for the ionized gas can be obtained once the electron temperature T_e is derived from the ratio of auroral to nebular emission lines, such as $[\text{O III}]\lambda\lambda 4959, 5007/[\text{O III}]\lambda 4363$. However, auroral lines are intrinsically faint, in particular in the metal rich galaxies, since the electron temperature decreases due to efficient cooling by metal lines. Hence, detection of such lines in high- z galaxies is not feasible with current facilities except for strongly lensed galaxies (Yuan & Kewley 2009). Alternatively, abundance indicators using strong emission lines are widely used to determine the metallicity, being calibrated with the T_e method and/or photoionization models. One of the most commonly used indicators is R_{23} (Pagel et al. 1979), which is defined as $\log R_{23} \equiv \log([[\text{O II}]\lambda 3727 + [\text{O III}]\lambda 4959 + [\text{O III}]\lambda 5007]/H\beta)$. However, R_{23} cannot be applied to our sample either, due to the lack of required emission lines. Here we use instead the N2 index (Storchi-Bergmann et al. 1994) defined as $\text{N2} \equiv \log([\text{N II}]\lambda 6583/H\alpha)$. Since $H\alpha$ and $[\text{N II}]\lambda 6583$ are close to each other, the N2 index has the advantage of being insensitive to dust extinction and flux calibration, though the origin of nitrogen is rather complicated.

Metallicities derived from different calibrations are known to show (almost systematic) discrepancies in the mass-metallicity relation of the local star-forming galaxies (Tremonti et al. 2004, hereafter T04) of up to $\simeq 0.5$ dex (Ellison 2006; Kewley & Ellison 2008). Thus, it is essential to derive metallicities in a consistent way, as later we will compare the metallicities of our *sBzK* sample with those of galax-

ies at different redshifts drawn from the literature. Based on Kewley & Dopita (2002), Kobulnicky & Kewley (2004, hereafter KK04) derived an analytical expression for the conversion of N2 into $12 + \log(\text{O}/\text{H})$ that is consistent with the R_{23} calibration. The relation is expressed as:

$$\begin{aligned} 12 + \log(\text{O}/\text{H}) = & 7.04 + 5.28X_{\text{NII}} + 6.28X_{\text{NII}}^2 + 2.37X_{\text{NII}}^3 \\ & - \log q(-2.44 - 2.01X_{\text{NII}} \\ & - 0.325X_{\text{NII}}^2 + 0.128X_{\text{NII}}^3) \\ & + 10^{X_{\text{NII}}-0.2} \log q(-3.16 + 4.65X_{\text{NII}}), \end{aligned} \quad (5)$$

where $X_{\text{NII}} \equiv \log \text{EW}([\text{N II}]\lambda 6583)/\text{EW}(H\alpha)$ and q is the ionization parameter. Since the EWs of $[\text{N II}]$ and $H\alpha$ were derived by assuming a flat continuum, EWs in X_{NII} can be replaced by the corresponding emission line fluxes. According to KK04, the ionization parameter is derived iteratively from the ionization-sensitive index $\log O_{32} = \log([\text{O III}]\lambda 4959 + [\text{O III}]\lambda 5007)/[\text{O II}]\lambda 3727$. However, once more also O_{32} cannot be derived for galaxies in our sample, as some of the required lines are not available. We have then assumed a constant ionization parameter, an assumption that is justified as follows after comparing metallicities from the N2 index and those from the R_{23}/O_{32} index. To derive metallicities from both indices, we used emission line fluxes for 75,561 star-forming galaxies in the SDSS DR4 archive compiled by MPA/JHU collaboration¹². Then we calculated $12 + \log(\text{O}/\text{H})$ for these SDSS star-forming galaxies using Equation (5) and by the relation (KK04):

$$\begin{aligned} 12 + \log(\text{O}/\text{H}) = & 9.11 - 0.218x - 0.0587x^2 \\ & - 0.330x^3 - 0.199x^4 \\ & - y(0.00235 - 0.01105x - 0.051x^2 \\ & - 0.04085x^3 - 0.003585x^4), \end{aligned} \quad (6)$$

where $x = \log(R_{23})$ and $y = \log(O_{32})$.

Figure 6 shows the correlation between these two metallicity calibrators, with different ionization parameters $q = 1 \times 10^7$, 2×10^7 , 3×10^7 and 4×10^7 . This figure indicates that a value $q = 3 \times 10^7$ makes the two metallicities to agree for galaxies near the peak of the metallicity distribution, while the N2 calibration tends to overestimate the metallicity for $12 + \log(\text{O}/\text{H})_{R_{23}} \lesssim 8.8$. Given that the metallicities of our sample are generally large, $12 + \log(\text{O}/\text{H}) > 8.8$ (see below), we have adopted $q = 3 \times 10^7$ in Equation (5).

The resulting gas-phase oxygen abundances of our *sBzKs* are listed in Table 6. Although D3a-8608 has $[\text{N II}]/H\alpha > 0.7$, which indicates that the ionization may be dominated by an AGN (Swinbank et al. 2004), we derived its metallicity with the same equation, just for a reference. The average value of $12 + \log(\text{O}/\text{H})$ in our sample is 8.97 ± 0.21 excluding objects with upper limits and AGN dominated features, i.e., D3a-3287, D3a-4626, D3a-8608, and D3a-11391.

4.4. Dynamical Masses

Thanks to the higher spectral resolution ($R \simeq 1500$) of the SINFONI instrument, $H\alpha$ and $[\text{N II}]$ emission lines are well resolved, which enables us to measure the velocity width of individual objects. In the following we refer

¹² <http://www.mpa-garching.mpg.de/SDSS/>

to such velocity width as the *velocity dispersion*, although we are aware that in many cases it is likely due mostly to ordered rotation rather than true velocity dispersion (cf. Förster Schreiber et al. 2009). The measured velocity dispersions, after deconvolving in quadrature the instrumental resolution ($R = 1500$, or $\sigma_{\text{instrument}} = 85 \text{ km s}^{-1}$), are listed in Table 3. Then dynamical masses are derived using the equation (e.g., Binney & Tremaine 1987; Pettini et al. 2001):

$$M_{\text{dyn}} = \frac{5r_{\text{hl}}\sigma^2}{G}, \quad (7)$$

where for the half-light radius, r_{hl} we have adopted 6 kpc, i.e., the average value for the *sBzKs* in the K20 survey measured by Daddi et al. (2004b) on the *HST/ACS* F850LP-band image. This assumes that the $\text{H}\alpha$ emission comes from H II regions which are virialized within the potential well of the host galaxy, and that the spatial distribution of H II regions represents that of underlying light distribution. Dynamical masses derived in this way are listed in Table 7. Note that the velocity dispersion of D3a-4751 is less than the width of the instrumental profile, hence the velocity dispersion could have large uncertainty. The average of dynamical masses of 8 *sBzKs* with measured velocity dispersion is $\langle M_{\text{dyn}} \rangle = 2.3 \times 10^{11} M_{\odot}$ with 1σ scatter of $1.5 \times 10^{11} M_{\odot}$.

There are several possible sources of error in these estimates of the dynamical mass. The half-light radius which is assumed as constant must actually vary from one object to another. For example, in the case of the UV-selected galaxies studied by Erb et al. (2006b) the half-light radius varies by more than a factor of 5 from, $\sim 2 \text{ kpc}$ to $\sim 11 \text{ kpc}$ while the average is $\simeq 6 \text{ kpc}$. In a recent integral field $\text{H}\alpha$ spectroscopic survey of $z \simeq 2$ galaxies Förster Schreiber et al. (2009) find an average half-light radius of the $\text{H}\alpha$ emitting region of 3.4 kpc. If we adopt this value, the derived dynamical masses would be 0.6 times smaller than estimated above. The numerical factor in Equation (7) could also be a dominant source of uncertainty. The adopted value of 5 is valid for a sphere of uniform density, while the actual value of this factor depends on various parameters, such as the mass distribution within the galaxy, its velocity structure, and the relative contributions of rotation and pressure support for star-forming regions (Lanzoni & Ciotti 2003). Considering a disk geometry, Erb et al. (2006b) used 3.4 for the factor and obtained the average dynamical mass of UV-selected star-forming galaxies at $z \simeq 2$ of $M_{\text{dyn}} \simeq 1 \times 10^{11} M_{\odot}$ with 1σ scatter of $8.5 \times 10^{10} M_{\odot}$, after accounting for differences in scaling factor. As mentioned above, several of these *sBzKs* are likely to be rotating disks (e.g., Genzel et al. 2006), in which case the reported dynamical masses are overestimated by $\sim 50\%$. Therefore, the dynamical masses derived here could be taken as upper limits unless half-light radius is larger than 6 kpc.

For most of the objects these dynamical masses are ~ 2 – 3 times larger than the stellar masses, which in principle could be due to the presence of large gas masses (e.g., Daddi et al. 2008, 2010). However, spatially resolved integral field spectroscopy would be required for a more robust determination of the dynamical mass (e.g., Förster Schreiber et al. 2009).

4.5. Composite Spectrum of *sBzKs*

The composite spectrum shown in Figure 7 is made by stacking the 6 SINFONI spectra of *sBzKs* with $\text{H}\alpha$ detection and without AGN features, where $\text{H}\alpha$ and $[\text{N II}]\lambda 6583$ are well resolved. Note that we have excluded D3a-11391

which shows broad-line $\text{H}\alpha$ component as well as the *sBzKs* with higher $[\text{N II}]/\text{H}\alpha$ ratio as AGN candidates. Individual spectra were corrected to the rest-frame wavelength and then stacked with weights inversely proportional to the square of the 1σ rms versus wavelength. Motivated by the finding of a broad-line $\text{H}\alpha$ component in the stacked spectra of $z \simeq 2$ star-forming galaxies in the SINS survey (Shapiro et al. 2009), we also fit multiple Gaussian functions to the composite spectrum, with and without a broad $\text{H}\alpha$ component, though due to the shorter exposure time for each object and smaller number of spectra used for the stacking, the S/N is lower than that of the SINS stacked spectrum. Including broad $\text{H}\alpha$ component makes the reduced- χ^2 of the fit about 25% smaller. The best fit Gaussian profiles are also shown in Figure 7.

The spectral properties derived from this composite spectrum are $\text{EW}(\text{H}\alpha) = 102 \text{ \AA}$, $\text{EW}([\text{N II}]\lambda 6583) = 41 \text{ \AA}$, and $\text{FWHM} = 350 \text{ km s}^{-1}$ or $\sigma = 150 \text{ km s}^{-1}$ for the fitting without a broad $\text{H}\alpha$ component, and $\text{EW}(\text{H}\alpha; \text{narrow}) = 50 \text{ \AA}$, $\text{EW}(\text{H}\alpha; \text{broad}) = 54 \text{ \AA}$, $\text{EW}([\text{N II}]\lambda 6583) = 24 \text{ \AA}$, $\text{FWHM}(\text{narrow}) = 170 \text{ km s}^{-1}$ or $\sigma(\text{narrow}) = 73 \text{ km s}^{-1}$ and $\text{FWHM}(\text{broad}) = 870 \text{ km s}^{-1}$ or $\sigma(\text{broad}) = 370 \text{ km s}^{-1}$ for the fitting with a broad $\text{H}\alpha$ component. Velocity dispersions above, are corrected for the instrumental resolution. Gas-phase oxygen abundances derived from the narrow line components of the composite spectrum can be calculated as $12 + \log(\text{O}/\text{H}) = 9.12$ and 9.03 ; the line widths lead to a dynamical mass of $M_{\text{dyn}} = 3.7 \times 10^{10} M_{\odot}$ and $1.5 \times 10^{11} M_{\odot}$ for the fittings with and without a broad component, respectively. If the broad component is real, the dynamical mass is a factor ~ 2 lower than the average stellar mass of the galaxies used for the stack ($7.6 \times 10^{10} M_{\odot}$). However, stellar masses have been derived here assuming a straight Salpeter IMF, with most of the mass being provided by low-mass stars. Turning from a bottom-heavy IMF, to a bottom-light one such as the IMF of Chabrier (2003), the average stellar mass drops to $4.5 \times 10^{10} M_{\odot}$, quite close to the estimated dynamical mass, and we note that a bottom-light IMF appears to be more appropriate to account for the observed mass to light ratio of local galaxies (e.g., Renzini 2005). In addition, we may have somewhat overestimated stellar masses as our SED fits are based on stellar population models that do not incorporate the TP-AGB phase of stellar evolution. We conclude that the discrepancy between our dynamical and stellar masses is primarily a result of the assumed IMF, and regard the dynamical mass derived including the broad $\text{H}\alpha$ component as quite plausible and close to the actual stellar mass as well.

5. DISCUSSION

5.1. *sBzKs* with and without $\text{H}\alpha$ Detection

In most cases, non-detection of $\text{H}\alpha$ could well be due to a combination of bad weather, poor seeing, mis-alignment during the blind offset, and bad transmission or strong OH emission at the wavelength of the lines. However, it is interesting to see whether there are systematic differences in colors and physical properties between *sBzKs* with and without $\text{H}\alpha$ detection. In Figure 8 the $(B-z)$ – $(z-K)$ color-color diagram for the objects in our K -selected catalog is shown, using different symbols for $\text{H}\alpha$ detected and non-detected objects. $\text{H}\alpha$ detected *sBzKs* have on average $\sim 0.15 \text{ mag}$ bluer BzK colors than those without $\text{H}\alpha$ detection, which indicates a systematically lower dust extinction because the reddening vector runs parallel to the diagonal line separating *sBzKs* from the other objects (Daddi et al. 2004a). $\text{H}\alpha$ detected *sBzKs* also appears

to be slightly brighter in K -band compared to those without $H\alpha$ detections. Therefore, $H\alpha$ detections seem to be biased in favor of more massive, but less extinguished objects.

The reddening $E(B-V)$ from Equation (1) and the extinction corrected SFRs derived from the flux in the rest-frame UV (observed-frame B -band) according to the recipe in Daddi et al. (2004a) are plotted in Figure 9 as a function of stellar masses derived from Equation (2). There are no significant differences in stellar masses (~ 0.1 dex) and SFRs (20%, but uncertainties are large) between $H\alpha$ detections and non-detections, while the average reddening is 0.1 mag higher for the $H\alpha$ non-detections. Therefore, the primary factor affecting the detectability of $H\alpha$ emission lines from *sBzKs* appears to be the amount of dust extinction. This is also seen in Hayashi et al. (2009) where most of *sBzKs* with non-detected emission lines have redder *BzK* colors and large $E(B-V)$ values, $\gtrsim 0.5$.

5.2. Comparison with Other $z \simeq 2$ $H\alpha$ Spectroscopic Survey

Figure 10 compares K -band magnitudes, stellar masses, reddenings, $H\alpha$ fluxes and $H\alpha$ luminosities of our *BzK* sample with those from other $H\alpha$ spectroscopic surveys at $z \simeq 2$. The $H\alpha$ fluxes and luminosities are not corrected for extinction. The galaxy samples include the rest-frame UV-selected BX/BM galaxies (Erb et al. 2006b,c), rest-frame optically selected *sBzK* galaxies (Hayashi et al. 2009), and the $z \simeq 2$ star-forming galaxies observed by the SINS survey (Förster Schreiber et al. 2009) which includes BX/BM galaxies as well as *BzK*-selected galaxies. Compared to the other $H\alpha$ detected star-forming galaxies, our sample contains only K -bright, massive objects mainly because of the brighter K -band limiting magnitude of the imaging survey from which they have been culled (K06). Apart from that, galaxies in our sample are distributed over similar ranges of physical properties (e.g., mass, SFR, extinction) compared to other samples based on rest-frame optical selections. In contrast, BX/BM galaxies tend to be less obscured by dust as expected from their selection technique and the fraction of objects with strong $H\alpha$ flux and luminosity (e.g., $f_\lambda(H\alpha) \gtrsim 10^{-16} \text{erg s}^{-1} \text{cm}^{-2}$ and $L(H\alpha) \gtrsim 2 \times 10^{42} \text{erg s}^{-1}$) appears to be smaller than among *sBzKs*. Since dust extinction is not corrected in Figure 10 (c) and (d), the difference between the rest-frame optically-selected population and rest-frame UV-selected one would become even larger once extinction correction is applied.

5.3. Comparison of Star-formation Rates from UV, $H\alpha$, and Mid-infrared

In §4.2 we have derived $H\alpha$ star-formation rates with extinction correction following, in which the dust extinction towards H II regions is larger than that resulting from the SED fit to the stellar continuum. To check the validity of this extinction correction, SFRs from $H\alpha$ are compared in Figure 11 with those derived from the MIR and the UV using the same procedure as in Daddi et al. (2007a), which is reproduced here below. Following the conversion of Kennicutt (1998), the IR SFR, or SFR(IR), is derived from the total IR luminosity (L_{IR}) as

$$\text{SFR(IR)} [M_\odot \text{yr}^{-1}] = 1.73 \times 10^{-10} L_{\text{IR}} [L_\odot]. \quad (8)$$

The total IR luminosity is derived from the luminosity-dependent SED library of Chary & Elbaz (2001) by using the rest-frame $8 \mu\text{m}$ luminosity ($L_{8\mu\text{m}}$), where the flux density at $24 \mu\text{m}$ from *Spitzer*/MIPS is used as a proxy of the rest-frame

$8 \mu\text{m}$, since $24 \mu\text{m}$ corresponds to $\simeq 8 \mu\text{m}$ at $z \simeq 2$. The conversion from $L_{8\mu\text{m}}$ to L_{IR} is then

$$\log \left(\frac{L_{\text{IR}}}{L_\odot} \right) = 1.50 \log \left(\frac{\nu L_{8\mu\text{m}}}{L_\odot} \right) - 4.31, \quad (9)$$

if $\log(\nu L_{8\mu\text{m}}) > 9.75$, and

$$\log \left(\frac{L_{\text{IR}}}{L_\odot} \right) = 0.93 \log \left(\frac{\nu L_{8\mu\text{m}}}{L_\odot} \right) + 1.23, \quad (10)$$

if $\log(\nu L_{8\mu\text{m}}) < 9.75$ (Daddi et al. 2007a). The UV SFR, or SFR(UV), is derived from rest-frame 1500 \AA luminosity (L_{1500}) by using equation (5) of Daddi et al. (2004a), i.e.,

$$\text{SFR(UV)} [M_\odot \text{yr}^{-1}] = 1.13 \times 10^{-28} L_{1500} [\text{ergs s}^{-1}]. \quad (11)$$

The observed-frame B -band is used to derive L_{1500} after applying a K -correction based on the redshift and the UV-slope of each object. Finally, the reddening $E(B-V)$ from Equation (1) is used for the correction of dust extinction to derive the extinction-corrected SFR. Figure 11(a) compares the total SFRs derived from summing SFR(UV) uncorrected for extinction and SFR(IR), and SFRs derived from $H\alpha$ luminosities with the extinction correction described in §4.2. These two sets of SFRs agree well with each other, with a few exceptions. One *sBzK*, D3a-11391, having much lower $\text{SFR}(H\alpha) = 40 M_\odot \text{yr}^{-1}$ compared to $\text{SFR}(\text{UV}+\text{IR}) = 1100 M_\odot \text{yr}^{-1}$ is a MIR-excess object (Daddi et al. 2007b), defined as an object having $\text{SFR}(\text{UV}+\text{IR}) \gtrsim 3$ times higher than the SFR(UV) corrected for extinction. The object has extinction corrected SFR(UV) of $120 M_\odot \text{yr}^{-1}$ which is also much smaller than SFR(UV+IR). Daddi et al. (2007b) suggested that MIR-excess objects could be hosting an obscured AGN, being almost completely opaque in the UV due to dust extinction, but emitting strongly in the MIR from hot dust surrounding the nuclei.

The outliers showing very large excess in $H\alpha$ SFR, D3a-5814 and D3a-6397, are possibly due to overestimates in $E(B-V)$ from the SED fitting. The $E(B-V)$ of these 2 *sBzKs* from *BzK* colors are smaller than those from SED fitting (Table 1 and 4). For large values of $E(B-V)$, even a relatively small difference in $E(B-V)$ makes a large difference in the resulting $H\alpha$ SFR.

In the original Calzetti's recipes for extinction correction it is suggested that the emission lines from H II regions suffer more extinction than the stellar continuum by a constant factor of 2.3, or $E(B-V)_{\text{star}} = 0.44 E(B-V)_{\text{gas}}$ (Calzetti 2001). If we simply use $E(B-V)_{\text{star}}$ from SED fitting as $E(B-V)_{\text{gas}}$, i.e., no additional obscuration toward H II regions, then the resulting $H\alpha$ SFRs are lower than those derived in §4.2 by factors of ~ 2 to 5. On the other hand, if $E(B-V)_{\text{star}} = 0.44 E(B-V)_{\text{gas}}$ is used for extinction correction following Calzetti (2001), it generally overestimates the $H\alpha$ SFR up to factor of ~ 2 . $H\alpha$ SFRs derived by Hayashi et al. (2009) by using $E(B-V)_{\text{gas}}$ according to the Calzetti's recipes are overestimated by a large factor compared to the UV SFRs with extinction correction by $E(B-V)_{\text{star}}$. On the other hand, extinction corrected $H\alpha$ SFRs and UV SFRs agree reasonably well for the UV-selected $z \simeq 2$ galaxies (Erb et al. 2006c) in which the amount of dust extinction is not large on average. This suggests that original Calzetti law could produce over-correction at least for heavily obscured galaxies like *sBzKs*. Therefore, the two cases above, $E(B-V)_{\text{gas}} = E(B-V)_{\text{star}}$ and $E(B-V)_{\text{gas}} = E(B-V)_{\text{star}}/0.44$, bracket the $H\alpha$ SFR derived in §4.2 by using the recipe of

Cid Fernandes et al. (2005), and additional extinction toward H II regions depending on the amount of extinction of stellar components could be justified in correcting the H α fluxes.

In Figure 11 UV SFR corrected for dust extinction and H α SFR are plotted. After extinction correction for the H α luminosities, both SFRs agree reasonably well except for D3a-5814 which is also an outlier in Figure 11(a). The other outlier in Figure 11(a), D3a-6397, is not an outlier in Figure 11(c), possibly because of the smaller difference between the $E(B-V)$ from SED fitting and that from BzK color, compared to that of D3a-5814.

5.4. Broad H α Emission Lines and Super Massive Black Holes

As shown in the above sections, D3a-11391 is the only galaxy in our sample of H α detected BzK sources that would be classified as a MIR-excess galaxy following Daddi et al. (2007b). This galaxy shows a broad H α component in addition to the narrow component, supporting the idea that it contains a powerful AGN. The velocity width of D3a-11391, $\text{FWHM} \simeq 2450 \text{ km s}^{-1}$, is in between that of stacked SINS galaxies at $z \simeq 2$ (Shapiro et al. 2009) with $M_* \gtrsim 10^{11} M_\odot$ ($\simeq 2200 \text{ km s}^{-1}$) and that of stacked SINS AGNs ($\simeq 2900 \text{ km s}^{-1}$). Many of the most massive galaxies in Shapiro et al. (2009) sample are also MIR excess galaxies. Swinbank et al. (2004) also detected a broad-line component in the stacked spectrum of submillimeter galaxies (SMGs), with $\text{FWHM} = 1300 \text{ km s}^{-1}$ for the stacked spectrum of the whole SMG sample, and $\text{FWHM} = 890 \text{ km s}^{-1}$ for that of the SMGs with no sign of an AGN component. Moreover, some individual SMGs show a broad H α with $\text{FWHM} \simeq 2000\text{--}4000 \text{ km s}^{-1}$ (Swinbank et al. 2004; Alexander et al. 2008). The velocity width of the broad-line component in our stacked spectrum, $\text{FWHM} = 870 \text{ km s}^{-1}$ (cf. §4.5) is close to the velocity width of the SMGs without obvious signs of AGN activity.

Although strong supernova-driven winds can produce a velocity width of $\text{FWHM} > 2000 \text{ km s}^{-1}$, it seems difficult to explain the MIR-excess as due to supernova remnants because supernovae are directly related to the star-formation activity which would also produce UV and H α emissions, consistent with the MIR emission. Thus, the object could be hosting an AGN at the center and the MIR-excess can be due to the surrounding dust torus which absorbs the UV emission from the central nucleus. Although typical MIR-excess galaxies are expected to contain very obscured, often Compton thick AGNs, the broad H α emission can be explained as a leak from the broad-line region (BLR) around the central nucleus, which would still be observable in the optical/NIR where the optical depths is lower than in the UV. Alternatively, H α photons in the broad component could have been scattered into the line-of-sight by either electrons or dust particles. Unfortunately, there are no X-ray data for this object, and the H α –X-ray diagnostics discussed in Alexander et al. (2008) cannot be applied. In the following discussion, we assume that the broad-line emission is not dominated by scattered light but is seen directly.

By using the measured H α luminosity and the width of the broad line and assuming that it is coming from an AGN, we attempt here a rough estimate of the virial mass of the central super massive black hole (SMBH) by adopting the relation

provided by Greene & Ho (2005):

$$M_{\text{BH}} = (2.0_{-0.3}^{+0.4}) \times 10^6 \times \left(\frac{L_{\text{H}\alpha}}{10^{44} \text{ ergs s}^{-1}} \right)^{0.55 \pm 0.02} \left(\frac{\text{FWHM}_{\text{H}\alpha}}{10^3 \text{ km s}^{-1}} \right)^{2.06 \pm 0.06} M_\odot, \quad (12)$$

or the relation by Kaspi et al. (2005) as converted by Greene & Ho (2005) for the H α luminosity and width:

$$M_{\text{BH}} = (1.3 \pm 0.3) \times 10^6 \times \left(\frac{L_{\text{H}\alpha}}{10^{44} \text{ ergs s}^{-1}} \right)^{0.57 \pm 0.06} \left(\frac{\text{FWHM}_{\text{H}\alpha}}{10^3 \text{ km s}^{-1}} \right)^{2.06 \pm 0.06} M_\odot. \quad (13)$$

For the broad component of D3a-11391, $L_{\text{H}\alpha} = 7.6 \times 10^{42} \text{ ergs s}^{-1}$ and $\text{FWHM}_{\text{H}\alpha} = 2450 \text{ km s}^{-1}$ lead to $M_{\text{BH}} \simeq 3 \times 10^7 M_\odot$ by averaging the values from these two equations. If the geometry of BLR is disk-like, the average correction factor for the inclination would be $\simeq 2.7$ (McLure & Dunlop 2002; Alexander et al. 2008), which gives $M_{\text{BH}} \simeq 9 \times 10^7 M_\odot$. The resulting value is $\simeq 2\text{--}3$ times smaller than the average SMBH mass of broad-line SMGs at $z \simeq 2$ (Alexander et al. 2008), and a factor $\gtrsim 10$ smaller than that of optically selected QSOs in SDSS at $z = 1.8\text{--}2.1$ (McLure & Dunlop 2004; Alexander et al. 2008). On the other hand, SINS galaxies with similar stellar mass have $\simeq 3$ times smaller black hole mass compared to what estimated here for D3a-11391 (Shapiro et al. 2009). Dust extinction for the broad-line H α emission is not considered here since H β emission line is out of the observed wavelength range. If we assume the same amount of extinction as that for the host galaxy ($A_V = 1$), it would increase the virial black hole mass by about a factor of 2.

Rest-frame 2–10 keV X-ray luminosity can be inferred from rest-frame $8 \mu\text{m}$ luminosity assuming that the emission from AGN dominates at $8 \mu\text{m}$ (Lutz et al. 2004; Alexander et al. 2008). Since $24 \mu\text{m}$ corresponds to rest-frame $8.7 \mu\text{m}$ at $z = 1.774$, MIPS $24 \mu\text{m}$ flux can be used as a proxy of rest-frame $8 \mu\text{m}$ luminosity. The flux of D3a-11391 is $\sim 400 \mu\text{Jy}$ at $24 \mu\text{m}$, corresponding to $\nu L_{8 \mu\text{m}} \simeq 10^{45} \text{ ergs s}^{-1}$, which is translated into an absorption corrected 2–10 keV luminosity of $L_{2\text{--}10\text{keV}} \simeq 10^{44} \text{ ergs s}^{-1}$ by using the same method as in Alexander et al. (2005). Alternatively, the H α luminosity can be also used to derive 2–10 keV luminosity (Ward et al. 1988), and from Figure 5 of Ward et al. (1988) we derive $L_{2\text{--}10\text{keV}} \simeq 10^{44} \text{ ergs s}^{-1}$, in agreement with the estimate from the $8 \mu\text{m}$ luminosity. Given that a mass-accretion of $1 M_\odot \text{ yr}^{-1}$ corresponds to $L_{2\text{--}10\text{keV}} \simeq 2.2 \times 10^{44} \text{ ergs s}^{-1}$, the mass-accretion rate of matter to the central SMBH of D3a-11391 can be estimated as $\simeq 0.5 M_\odot \text{ yr}^{-1}$. While this estimate is obviously affected by large uncertainties, we note that this SMBH accretion rate is about 1/2 of the value estimated for broad-line SMGs (Alexander et al. 2008) and one order of magnitude smaller than the typical value of QSOs at $z = 1.8\text{--}2.1$ (McLure & Dunlop 2004; Alexander et al. 2008).

Then we can proceed further, and crudely estimate the Eddington factor, η , by comparing M_{BH} and the accretion rate (Figure 2 of Alexander et al. 2008). For D3a-11391 this gives $\eta \simeq 0.3\text{--}0.9$, depending on the assumed geometry, somewhat higher than the typical Eddington ratio of broad-line SMGs and lower than the average of SINS galaxies. However, uncertainties in both black hole mass and mass-accretion rate are large.

A broad-line component with $\text{FWHM} = 870 \text{ km s}^{-1}$ was also detected our stacked spectrum of the remaining *BzK* galaxies (Fig. 7), although not with high significance. Its velocity width is not as large as that of BLRs, but rather similar to that of narrow-line Seyfert galaxies. Proceeding in the same way as for D3a-11391, we then estimate the black hole mass, X-ray luminosity, accretion rate and Eddington factor for the *average* galaxy represented by the stacked spectrum. We then obtain $M_{\text{BH}} = 3 \times 10^6 M_{\odot}$ or $7 \times 10^6 M_{\odot}$, respectively for spherical and disk-like geometry, $L_{2-10\text{keV}} \simeq 5 \times 10^{43} \text{ ergs s}^{-1}$, an accretion rate of $0.2 M_{\odot} \text{ yr}^{-1}$, and $\eta \gtrsim 1$. Here we have used the average redshift ($z = 1.96$), average $\text{H}\alpha$ luminosity ($3.4 \times 10^{42} \text{ ergs s}^{-1} \text{ cm}^{-2}$) and average $24\mu\text{m}$ flux ($156\mu\text{Jy}$) of the galaxies in the stack. It is also assumed that the whole $24\mu\text{m}$ flux comes from an obscured AGN, which would overestimate the rest-frame $8\mu\text{m}$ luminosity. By inferring the X-ray luminosity from the broad $\text{H}\alpha$ luminosity we get $L_{2-10\text{keV}} \simeq 3 \times 10^{43} \text{ erg s}^{-1}$, quite consistent with the value estimated from the $8\mu\text{m}$ luminosity, and similar to the value estimated by Daddi et al. (2007b) for the MIR-excess galaxies on the basis of X-ray stacking.

5.5. Mass-Metallicity Relation

The gas-phase oxygen abundances of the galaxies in the present sample as derived from Equation (5) are plotted as a function of stellar mass in Figure 12. Error bars for stellar mass are set to 0.3 dex, as the typical uncertainty of our estimates. AGN candidates, i.e., those showing large $[\text{N II}]/\text{H}\alpha$ (> 0.7) ratios, are also plotted in Figure 12 as open squares and circles. The metallicity derived from the stacked spectrum (with and without the broad line component) is also shown along with the average stellar mass of the stacked galaxies (star symbols). The solar oxygen abundance is indicated with the dashed line, hence almost all galaxies in the present sample appear to have super-solar ISM abundances. However, the absolute values of the oxygen abundances should be taken with caution having been obtained indirectly from the $[\text{N II}]/\text{H}\alpha$ ratio. For example, by comparing various indicators of gas-phase oxygen abundance, including the T_e method, Shi et al. (2005) using $[\text{O III}]\lambda 4363$ found that in the luminosity-metallicity (L - Z) relation of the local blue compact dwarfs, there is a systematic offset between the L - Z relation derived from the T_e method and that from the R_{23} method, i.e., the method that we have used as a reference calibration by scaling the ionization parameter in the N2-based calibration (see §4.3). The R_{23} -based L - Z relation has a systematically higher zeropoint than the T_e -based one, thus the R_{23} method may overestimate the true oxygen abundance. Therefore, using the same calibrator is crucial to compare various observations as shown below.

T04 derived the M_* - Z relation in the local universe ($z \sim 0.1$) by using 53,000 star-forming galaxies from the SDSS DR2 release, and their M_* - Z relation can be used as the reference relation for $z \simeq 0$. However, their metallicity measurements are based on model fitting to multiple emission lines (Charlot & Longhetti 2001), and therefore are not directly comparable to our results derived from Equation (5). To cope with this problem, we have used SDSS DR4 data as described in §4.3, and multiplied their stellar masses by a factor 1.5 (to convert from Kroupa IMF to Salpeter IMF). Then the resulting M_* - Z relation for SDSS galaxies with R_{23}/O_{32} calibrated

abundances is fitted with the 2nd order polynomial,

$$\begin{aligned} 12 + \log(\text{O}/\text{H}) &= 1.0512 \\ &+ 1.3836 \log(M_*/M_{\odot}) \\ &- 0.0602 [\log(M_*/M_{\odot})]^2, \end{aligned} \quad (14)$$

which is finally used as the reference relation at $z \sim 0$ in Figure 13.

The M_* - Z relation for 57 star-forming galaxies from the GDDS/CFRS surveys (Savaglio et al. 2005) is then used as a reference at intermediate redshift, $z \simeq 0.7$. Since they used R_{23} as in KK04 to calibrate abundances and the Baldry & Glazebrook (2003) IMF, we convert only their stellar masses to those corresponding to the Salpeter IMF, by multiplying them by a factor 1.8.

In addition to the *sBzKs* in this study, we also consider masses and abundances of the following $z \sim 2$ objects: 6 distant red galaxies (DRGs) at $2.4 < z < 3.2$ (van Dokkum et al. 2004) where only one out of 6 presented in van Dokkum et al. (2004) is used here because 4 DRGs show obvious AGN features (broad-line and high $[\text{N II}]/\text{H}\alpha$ ratio), and for another object neither N2 nor R_{23} indicators could be used for a metallicity measurement; 87 UV-selected (BX/BM) star-forming galaxies at $\langle z \rangle = 2.26$ (Erb et al. 2006a) which are binned into 6 mass bins containing ~ 15 galaxies per bin; the Lyman-break galaxy MS1512-cB58 at $z = 2.73$ (Teplitz et al. 2000; Baker et al. 2004); and finally the average of 7 SMGs with $[\text{N II}]/\text{H}\alpha < 0.7$ at $\langle z \rangle = 2.4$ (Smail et al. 2004; Swinbank et al. 2004). The stellar masses are all corrected to the Salpeter IMF, taking gravitational lensing into account in the case of cB58. All gas-phase oxygen abundances are derived with the KK04 calibration by using the $[\text{N II}]/\text{H}\alpha$ emission line ratios as listed in the quoted references so to ensure full homogeneity with the *sBzK* abundances derived in this paper.

Figure 13 compares masses and abundances of *sBzKs* at $z \simeq 2$ to those of the objects mentioned above. Most *sBzKs* at $z \simeq 2$ are already enriched to abundances comparable to those of SDSS and GDDS/CFRS galaxies in the same stellar mass range, i.e., $\log M_* \gtrsim 10.5$. The ISM abundances of *sBzKs* appears to be consistent with those of $z \simeq 2$ galaxies of comparable mass, although selected according to different criteria (i.e., DRGs and SMGs), while the M_* - Z relation of UV-selected galaxies from Erb et al. (2006a) tend to show slightly lower ($\simeq 0.15$ – 0.2 dex) abundances at a given stellar mass. This offset from the M_* - Z relation of UV-selected galaxies which is generated by the spectral stacking can be seen also when compared with the metallicities of the composite spectra of *sBzKs* at similar stellar mass. Since the metallicity uncertainties are rather large, this offset may not be very significant. Also Hayashi et al. (2009) have reported a $\simeq 0.2$ dex higher average metallicities of their *sBzKs* compared to UV-selected galaxies. Our metallicities are closer to those of Hayashi et al. (2009) than to those of Erb et al. (2006a), though uncertainties are large. Hayashi et al. (2009) also mentioned a possible bias towards higher metallicity objects, which would enable us to detect $[\text{N II}]$ emissions, hence to measure the metallicity. Indeed, their stacked spectrum of $[\text{N II}]$ undetected objects yields roughly the same metallicity as that of UV-selected galaxies.

Savaglio et al. (2005) noted the differential redshift evolution of the M_* - Z relation from $z \sim 0.7$ to $z = 0.1$, with the most massive galaxies at $z \sim 0.7$ ($\log M_* \gtrsim 10.3$) being already en-

riched to the ISM abundances of the local galaxies, while less massive galaxies start leaving the local M_* - Z relation already at redshift as low as $z \sim 0.1$. Our result extends this trend to higher redshifts, finding that at the high mass end the chemical enrichment was virtually complete by $z \sim 2$. This indicates that massive galaxies evolve faster than less massive galaxies, where star formation and ensuing chemical enrichment are slow and last longer, i.e., yet another manifestation of *downsizing*.

5.6. Relation between Stellar Masses and Specific Star-formation Rates

The correlation between SFR and stellar mass has been extensively investigated from the nearby universe to high redshift (e.g., Brinchmann et al. 2004; Daddi et al. 2007a; Elbaz et al. 2007; Noeske et al. 2007; Dunne et al. 2009; Pannella et al. 2009; Santini et al. 2009). In particular, the specific star-formation rate (SSFR), defined as the SFR per unit stellar mass, is widely used to quantify the contribution of current star-formation activity to the growth of the total stellar mass, i.e., of how efficiently stars are formed.

In Figure 14, we plot the SSFR as a function of stellar mass for *sBzK* galaxies with $H\alpha$ detection. Though the scatter and uncertainty in stellar mass are large, the average SSFR (in yr^{-1}) is around $\log \text{SSFR} \simeq -9$, and the SSFR- M_* does not show a detectable slope. A comparison of M_* -SSFR relations from different sources and at different redshifts is also shown in Figure 15. Data from literature are taken from Elbaz et al. (2007) for star-forming galaxies at $z \simeq 0$ in SDSS and $z \simeq 1$ in GOODS, as well as $z \simeq 2$ objects including *sBzKs* (Daddi et al. 2007a; Pannella et al. 2009), UV-selected star-forming galaxies (Erb et al. 2006c), DRGs (van Dokkum et al. 2004), and average of SMGs (Smail et al. 2004; Swinbank et al. 2004). Elbaz et al. (2007) and Daddi et al. (2007a) have estimated SFRs by adding extinction uncorrected rest-frame UV and IR luminosities to trace both absorbed and unabsorbed star formation. SFRs for *sBzKs* in the study of Pannella et al. (2009) have been derived from 1.4 GHz radio data (hence independent of extinction) finding excellent agreement with Daddi et al. (2007a). SFRs of DRGs and UV-selected star-forming galaxies at $z \simeq 2$ are derived from $H\alpha$ luminosities with extinction correction described in van Dokkum et al. (2004) and Erb et al. (2006c), respectively. The SFR of SMGs is derived from sub-mm emission. Since these SFRs are taken from the original papers, which besides different selection criteria have also used a variety of different observables (such as UV-luminosity, $H\alpha$ luminosity, FIR luminosity and radio luminosity), it is not a surprise to find even large systematic differences.

From low to high redshift, SSFRs at a given stellar mass increase systematically as shown by e.g., Elbaz et al. (2007), Daddi et al. (2007a) and Pannella et al. (2009). The *sBzKs* presented in this study distribute around the average SSFR- M_* relation for *sBzKs* in these two latter studies. One *sBzK* galaxy shows a SSFR as high as that typical of SMGs, and can be regarded as a real outlier, though it is also possible that its $H\alpha$ SFR may have been overestimated since the object shows an $H\alpha$ excess but appears normal in the SFR(UV)-SFR(IR) comparison (Figure 11). Note that the M_* -SSFR relations for SDSS star-forming galaxies at $z \sim 0$, $z \simeq 1$ and for *sBzKs* at $z \simeq 2$ have almost flat slopes, ranging from ~ 0 to -0.23 , while the distribution of UV-selected galaxies in Erb et al. (2006a) shows a much steeper slope. A steeper slope, but systematically higher SSFRs for *sBzKs* in the M_* -SSFR relation has

been also reported by Hayashi et al. (2009), having used $H\alpha$ SFRs. However, their $H\alpha$ SFR are systematically higher than SFRs from the UV, while no comparison with the total (e.g., UV+IR) SFR is available (see §4.2 and §5.3). On average, *sBzKs* in the present study, as well as in those of Daddi et al. (2007a), Pannella et al. (2009) and Hayashi et al. (2009), have higher SSFRs at the massive end compared to those for UV-selected galaxies.

An almost flat M_* -SSFR relation for $z \sim 2$ *BzK*-selected galaxies which is almost indistinguishable from that of Daddi et al. (2007a) shown in Figure 15 is indeed found by Dunne et al. (2009) and Pannella et al. (2009). The discrepancy with respect to other, steep M_* -SSFR relations is ascribed to selection effects (Dunne et al. 2009), e.g., the UV selection being biased against massive, highly obscured and intensively star-forming galaxies, and in addition to a systematic underestimate of the dust extinction with increasing mass (Pannella et al. 2009). Regarding the discrepancy of slopes between $H\alpha$ spectroscopic surveys, an uncertain extinction correction for $H\alpha$ from SED fitting might be one of the major causes. Larger spectroscopic samples, exploring a wider range of stellar masses and SFRs, and detecting of $H\beta$ in addition to the $H\alpha$ (so to estimate accurate dust extinctions from the Balmer decrement) would be crucial for an independent evaluation of the slope in M_* -SSFR relation at $z \simeq 2$. Our results, though relative to a very small sample, are in line with those of Dunne et al. (2009) and Pannella et al. (2009).

5.7. An Interpretation of the Mass-metallicity and Mass-SSFR Relations with Simple Evolutionary Population Synthesis Models

In this section we try to interpret the M_* - Z and M_* -SSFR relations with evolutionary population synthesis models. We use the PÉGASE.2 models that are also used for SED fitting to derive stellar masses and dust extinction parameters. These are one-zone models which neglect interactions and merging of galaxies, that are naturally expected in hierarchical structure formation scenario. They also neglect galactic winds driven by supernovae and/or AGN feedback, that are known to exist and are responsible for the metal enrichment of the intergalactic and intracluster media. Although a galaxy rarely evolves as is modeled by PÉGASE.2, its simple description may give us a starting point towards understanding the M_* - Z and M_* -SSFR relations, and indicate in which direction we should try to find more satisfactory solutions. A detailed comparison with the full numerical simulation is not the focus of this paper.

Two scenarios, the simple closed-box model and the infall model for chemical enrichment, are considered here with a Salpeter IMF from $0.1M_\odot$ to $120M_\odot$ and the B-series of chemical yields from Woosley & Weaver (1995). These models assume that a galaxy is initially a purely gas cloud with zero metallicity, $Z = 0$, and the SFR is assumed to be proportional to the gas mass (i.e., a Schmidt law with $n = 1$):

$$\text{SFR}(t) = \frac{1}{\tau_{\text{sf}}} M_{\text{gas}}(t), \quad (15)$$

where τ_{sf} is the star-formation timescale. Closed-box models assume no gas infall and all gas resides in the system at the beginning. This is the classical *monolithic collapse* scenario. In the infall models, initially all gas is assumed to be in an outer reservoir and falls into the inner star-forming region at

a rate of

$$\xi_{\text{infall}}(t) = \frac{1}{\tau_{\text{infall}}} \exp\left(-\frac{t}{\tau_{\text{infall}}}\right), \quad (16)$$

where τ_{infall} is the infall time scale. We use models with $\tau_{\text{sf}} = 0.1$ and 5 Gyr and we assume $\tau_{\text{sf}} = \tau_{\text{infall}}$ for infall models. Short time scale models with $\tau_{\text{sf}} = 0.1$ Gyr can successfully reproduce the color-magnitude (C-M) relations of elliptical galaxies in nearby clusters of galaxies (Kodama & Arimoto 1997), and long time scale models with $\tau_{\text{sf}} = 5$ Gyr can explain the photometric properties of nearby late type, Sb–Sc, galaxies (Arimoto et al. 1992; Fioc & Rocca-Volmerange 1997). Following KK04, the ISM oxygen abundance is derived from the gas-phase metal mass fraction using the relation:

$$12 + \log(\text{O}/\text{H}) = 12 + \log\left(\frac{Z}{29}\right), \quad (17)$$

assuming the solar abundance pattern reported by Anders & Grevesse (1989) and the solar oxygen abundance from Allende Prieto et al. (2001).

Figures 16 and 17 show that both the closed-box and the infall models with $\tau_{\text{sf}} = 0.1$ Gyr can roughly reproduce the locations of *sBzKs* and other populations of $z \simeq 2$ galaxies at the massive end of the M_* - Z relation and of the M_* -SSFR relation, with $100 \lesssim t \lesssim 500$ Myr ages and $10^{11} \lesssim M_{\text{total}}/M_{\odot} \lesssim 10^{12}$ of gas mass. This range of ages is also roughly consistent with the onset epoch of galactic winds needed by the models of Kodama & Arimoto (1997) to reproduce the C-M relations of elliptical galaxies in the Virgo and Coma clusters. On the other hand, models with longer time scale, e.g., $\tau_{\text{sf}} = 5$ Gyr, cannot fit both relations simultaneously. For example, $\tau_{\text{sf}} = 5$ Gyr infall models take $\gtrsim 5$ Gyr to reach the observed metallicities of $z \simeq 2$ galaxies, while the age of the universe at $z \simeq 2$ is only ~ 3.4 Gyr for the adopted cosmology. Only simple models can reproduce the distribution of *sBzKs* and $z \simeq 2$ galaxies in the M_* - Z relation with such long τ_{sf} . However, in the M_* -SSFR relation, it turns out that simple models with longer time scale require huge amount of initial gas, $M_{\text{total}} > 10^{12} M_{\odot}$, which is larger than typical stellar mass of the most massive early-type galaxies found in the local universe. Moreover, the ages and stellar masses mentioned above imply an average SFR $> 10^3 M_{\odot} \text{yr}^{-1}$, much in excess of the observed SFRs of galaxies in such mass range.

On the other hand, Equations (15) and (16) imply a secularly declining SFR, such that all galaxies are assumed to have started with their maximum SFR and to be caught at their minimum SFR. This assumption is especially doubtful at $z \sim 2$, where the SFR of many star-forming galaxies may actually increase with time, rather than decrease (Renzini 2009; Maraston et al. 2010).

The high SFRs in the *BzK* galaxies presented here require galaxies to host a large amount of molecular gas to be used for star formation. Recent millimeter and radio observations have been revealing that star-forming *BzK* galaxies indeed harbor large amount of CO molecules, hence also molecular hydrogen (Daddi et al. 2008, 2010; Dannerbauer et al. 2009). These CO observations as well as multi-wavelength SED analysis (Daddi et al. 2007a,b) suggest that the gas consumption or star-formation timescale could be up to 1 Gyr rather than 100 Myr inferred in this study. In the framework of PÉGASE.2 used here, $\tau \lesssim 1$ Gyr is in fact an upper limit in order to reproduce the observed M_* - Z and M_* -SSFR relations at the same time, still being consistent with Daddi et al. (2007a,

2008).

Again, note that closed-box or infall models are certainly oversimplifications over the real star-formation histories of galaxies. Recent numerical simulations favor continuous (albeit fluctuating) cold-stream accretion for the main driver of the galaxy growth, rather than short-lived starbursts (e.g., Dekel et al. 2009). Thus, infall models may capture this aspect, but the results must critically depend on the assumed evolution with time of the infall rate.

SMGs, which are outlier in the M_* -SSFR relation, require extremely young ages, a few 10 Myr, while in the M_* - Z relation they occupy nearly the same position as other $z \simeq 2$ star-forming galaxies. This is possibly due to vigorous, merger-driven starbursts rather than due to internal star-formation mode assumed in the one-zone PÉGASE.2 models. These violent star-formation processes could push a galaxy almost vertically (Feulner et al. 2005) in the M_* -SSFR diagram, with little change of its position in the M_* - Z diagram.

6. SUMMARY AND CONCLUSIONS

We have conducted NIR spectroscopic observations of 28 *sBzK* galaxies at $z \simeq 2$ and detected $\text{H}\alpha$ emissions from 14 of them. By using the $\text{H}\alpha$ and [N II] lines, we have derived $\text{H}\alpha$ SFRs and gas phase oxygen abundances. Stellar masses and reddening parameters have been also derived by SED fitting to the multi-wavelength photometric data. Our results are summarized as follows:

- Stellar masses and reddening parameters derived from SED fitting agree well with those derived by *BzK*-based recipe introduced by Daddi et al. (2004a).
- A comparison of SFRs from different indicators ($\text{H}\alpha$, extinction corrected UV, and UV+MIR) indicates that additional extinction towards H II regions over that derived from the SED fitting of the stellar continuum is required for the $\text{H}\alpha$ SFR to recover the total SFR inferred from UV+MIR. The required additional extinction is in agreement with the recipe proposed by Cid Fernandes et al. (2005).
- One object, D3a-11391, shows MIR-excess and a broad $\text{H}\alpha$ component with FWHM $\simeq 2500 \text{ km s}^{-1}$, as well as a narrow line component, suggesting that it may host an AGN, which would be highly obscured at UV and X-ray wavelengths. Although with large uncertainty, we have estimated the mass of the SMBH and its intrinsic X-ray luminosity following Alexander et al. (2008), obtaining $M_{\text{BH}} \simeq (3-9) \times 10^7 M_{\odot}$, depending on the assumed geometry of the accretion disk, and $L_{2-10\text{keV}} \simeq 10^{44} \text{ ergs s}^{-1}$. From these quantities, the mass accretion rate onto the central SMBH and Eddington factor are calculated as $\dot{M}_{\text{BH}} \simeq 0.5 M_{\odot} \text{yr}^{-1}$ and $\eta \simeq 0.3-0.9$, again depending on the geometry. These properties are in between those of normal star-forming galaxies and those of broad-line SMGs, indicating a possible evolutionary connection between normal UV/optical-selected galaxies, broad-line/MIR-excess *sBzKs*, and star-forming broad-line SMGs that may result from an accelerated growth of SMBH.
- Most of *sBzKs* presented here have already reached a metallicity similar to that of local star-forming galaxies of the same mass. They tend to have higher metallicity compared to UV-selected $z \sim 2$ galaxies, even at

the top mass end. This indicates that $sBzK$ s are on average a more evolved population compared to that of UV-selected galaxies at the same redshift.

- Specific SFRs of most $sBzK$ s are consistent with a tight M_* -SSFR correlation (Daddi et al. 2007a; Pannella et al. 2009), with a couple of outliers reaching very high SSFRs, similar to those of SMGs
- Within the framework of PÉGASE.2 closed-box or infall models, the M_* - Z and M_* -SSFR relations of $z \simeq 2$ $sBzK$ s can be reproduced simultaneously assuming a very short star-formation or infall timescale, $\tau \simeq 100$ Myr, and large gas mass at the beginning. However, the implied SFRs averaged over the life of the galaxies appears to be excessively large, suggesting that secularly declining SFRs may not be appropriate for star-forming galaxies at $z \sim 2$.

We thank the anonymous referee for providing the useful and constructive report. Part of the materials presented in this paper is from the Ph.D. thesis of MO at the Astronomy Department of the University of Tokyo. We thank Kentaro Motohara for providing the reduction pipeline used for the OHS/CISCO spectra and for giving advice about data reductions. Marcella Brusa is thanked for providing us upper limits for the XMM-Newton/Chandra fluxes and Ranga-Ram Chary is thanked for help with the MIPS $24 \mu\text{m}$ data. We thank the staffs of the Subaru telescope and of the VLT for supporting the observations. This work was supported in part by a Grant-in-Aid for Science Research (No. 19540245) by the Japanese Ministry of Education, Culture, Sports, Science and Technology. DMA thanks the Royal Society and Leverhulme Trust for financial support. AR express gratitude to the INAF - Osservatorio Astronomico di Bologna for its hospitality and support.

REFERENCES

- Alexander, D. M., Smail, I., Bauer, F. E., Chapman, S. C., Blain, A. W., Brandt, W. N., & Ivison, R. J. 2005, *Nature*, 434, 738
- Alexander, D. M., et al. 2008, *AJ*, 135, 1968
- Allende Prieto, C., Lambert, D. L., & Asplund, M. 2001, *ApJ*, 556, L63
- Anders, E., & Grevesse, N. 1989, *Geochim. Cosmochim. Acta*, 53, 197
- Arimoto, N., Yoshii, Y., & Takahara, F. 1992, *A&A*, 253, 21
- Baker, A. J., Tacconi, L. J., Genzel, R., Lehnert, M. D., & Lutz, D. 2004, *ApJ*, 604, 125
- Baldry, I. K., & Glazebrook, K. 2003, *ApJ*, 593, 258
- Baldwin, J. A., Phillips, M. M., & Terlevich, R. 1981, *PASP*, 93, 5
- Binney, J., & Tremaine, S. 1987, *Galactic Dynamics* (Princeton Univ. Press)
- Bonnet, H., et al. 2004, *ESO Messenger*, 117, 17
- Brinchmann, J., Charlot, S., White, S. D. M., Tremonti, C., Kauffmann, G., Heckman, T., & Brinkmann, J. 2004, *MNRAS*, 351, 1151
- Buat, V., Boselli, A., Gavazzi, G., & Bonfanti, C. 2002, *A&A*, 383, 801
- Calzetti, D. 2001, *PASP*, 113, 1449
- Chabrier, G. 2003, *PASP*, 115, 763
- Charlot, S., & Longhetti, M. 2001, *MNRAS*, 323, 887
- Chary, R., & Elbaz, D. 2001, *ApJ*, 556, 562
- Cid Fernandes, R., Mateus, A., Sodré, L., Stasińska, G., & Gomes, J. M. 2005, *MNRAS*, 358, 363
- Cimatti, A., et al. 2008, *A&A*, 482, 21
- Daddi, E., Cimatti, A., Renzini, A., Fontana, A., Mignoli, M., Pozzetti, L., Tozzi, P., & Zamorani, G. 2004a, *ApJ*, 617, 746
- Daddi, E., et al. 2004b, *ApJ*, 600, L127
- Daddi, E., et al. 2005, *ApJ*, 631, L13
- Daddi, E., et al. 2007a, *ApJ*, 670, 156
- Daddi, E., et al. 2007b, *ApJ*, 670, 173
- Daddi, E., Dannerbauer, H., Elbaz, D., Dickinson, M., Morrison, G., Stern, D., & Ravindranath, S. 2008, *ApJ*, 673, L21
- Daddi, E., et al. 2010, *ApJ*, 713, 686
- Dannerbauer, H., et al. 2006, *ApJ*, 637, L5
- Dannerbauer, H., Daddi, E., Riechers, D. A., Walter, F., Carilli, C. L., Dickinson, M., Elbaz, D., & Morrison, G. E. 2009, *ApJ*, 698, L178
- Dekel, A., et al. 2009, *Nature*, 457, 451
- Drory, N., Bender, R., & Hopp, U. 2004, *ApJ*, 616, L103
- Dunne, L., et al. 2009, *MNRAS*, 394, 3
- Eisenhauer, F., et al. 2003, *Proc. SPIE*, 4841, 1548
- Elbaz, D., et al. 2007, *A&A*, 468, 33
- Ellison, S. 2006, *The Fabulous Destiny of Galaxies: Bridging Past and Present*, 53
- Erb, D. K., Shapley, A. E., Pettini, M., Steidel, C. C., Reddy, N. A., & Adelberger, K. L. 2006a, *ApJ*, 644, 813
- Erb, D. K., Steidel, C. C., Shapley, A. E., Pettini, M., Reddy, N. A., & Adelberger, K. L. 2006b, *ApJ*, 646, 107
- Erb, D. K., Steidel, C. C., Shapley, A. E., Pettini, M., Reddy, N. A., & Adelberger, K. L. 2006c, *ApJ*, 647, 128
- Feulner, G., Gabasch, A., Salvato, M., Drory, N., Hopp, U., & Bender, R. 2005, *ApJ*, 633, L9
- Fioc, M., & Rocca-Volmerange, B. 1997, *A&A*, 326, 950
- Fioc, M., & Rocca-Volmerange, B. 1999, *astro-ph/9912179*
- Förster Schreiber, N. M., et al. 2009, *ApJ*, 706, 1364
- Genzel, R., et al. 2006, *Nature*, 442, 786
- Greene, J. E., & Ho, L. C. 2005, *ApJ*, 630, 122
- Hayashi, M., et al. 2009, *ApJ*, 691, 140
- Iwamuro, F., Motohara, K., Maihara, T., Hata, R., & Harashima, T. 2001, *PASJ*, 53, 355
- Kajisawa, M., et al. 2009, *ApJ*, 702, 1393
- Kaspi, S., Maoz, D., Netzer, H., Peterson, B. M., Vestergaard, M., & Jannuzi, B. T. 2005, *ApJ*, 629, 61
- Kauffmann, G., et al. 2003, *MNRAS*, 346, 1055
- Kennicutt, R. C. 1998, *ARA&A*, 36, 189
- Kewley, L. J., & Dopita, M. A. 2002, *ApJS*, 142, 35
- Kewley, L. J., & Ellison, S. L. 2008, *ApJ*, 681, 1183
- Kobulnicky, H. A., & Kewley, L. J. 2004, *ApJ*, 617, 240 (KK04)
- Kodama, T., & Arimoto, N. 1997, *A&A*, 320, 41
- Kong, X., et al. 2006, *ApJ*, 638, 72 (K06)
- Kriek, M., et al. 2006a, *ApJ*, 645, 44
- Kriek, M., et al. 2006b, *ApJ*, 649, L71
- Kriek, M., et al. 2007, *ApJ*, 669, 776
- Kriek, M., van der Wel, A., van Dokkum, P. G., Franx, M., & Illingworth, G. D. 2008a, *ApJ*, 682, 896
- Kriek, M., et al. 2008b, *ApJ*, 677, 219
- Kroupa, P. 2002, *Science*, 295, 82
- Lanzoni, B., & Ciotti, L. 2003, *A&A*, 404, 819
- Le Fèvre, O., et al. 2005, *A&A*, 439, 845
- Lilly, S. J., et al. 2007, *ApJS*, 172, 70
- Lutz, D., Maiolino, R., Spoon, H. W. W., & Moorwood, A. F. M. 2004, *A&A*, 418, 465
- Madau, P. 1995, *ApJ*, 441, 18
- Madau, P., Ferguson, H. C., Dickinson, M. E., Giavalisco, M., Steidel, C. C., & Fruchter, A. 1996, *MNRAS*, 283, 1388
- Magdis, G. E., Rigopoulou, D., Huang, J.-S., & Fazio, G. G. 2009, *MNRAS*, 391, 1768
- Maraston, C. 1998, *MNRAS*, 300, 872
- Maraston, C. 2005, *MNRAS*, 362, 799
- Maraston, C. et al. 2010, *ApJ*, submitted
- McCracken, H. J., et al. 2010, *ApJ*, 708, 202
- McLure, R. J., & Dunlop, J. S. 2002, *MNRAS*, 331, 795
- McLure, R. J., & Dunlop, J. S. 2004, *MNRAS*, 352, 1390
- Mignoli, M., et al. 2005, *A&A*, 437, 883
- Motohara, K., et al. 2001, *PASJ*, 53, 459
- Motohara, K., et al. 2002, *PASJ*, 54, 315
- Noeske, K. G., et al. 2007, *ApJ*, 660, L43
- Oke, J. B., & Gunn, J. E. 1983, *ApJ*, 266, 713
- Osterbrock, D. E., & Ferland, G. J. 2005, *Astrophysics of Gaseous Nebulae and Active Galactic Nuclei* (2nd ed.; Univ. Science Books)
- Pagel, B. E. J., Edmunds, M. G., Blackwell, D. E., Chun, M. S., & Smith, G. 1979, *MNRAS*, 189, 95
- Pannella, M., et al. 2009, *ApJ*, 698, L116
- Pettini, M., Shapley, A. E., Steidel, C. C., Cuby, J.-G., Dickinson, M., Moorwood, A. F. M., Adelberger, K. L., & Giavalisco, M. 2001, *ApJ*, 554, 981
- Poppo, P., et al. 2009, *A&A*, 494, 443
- Reddy, N. A., Erb, D. K., Steidel, C. C., Shapley, A. E., Adelberger, K. L., & Pettini, M. 2005, *ApJ*, 633, 748
- Renzini, A. 2005, *The Initial Mass Function 50 Years Later*, 327, 221
- Renzini, A. 2009, *MNRAS*, 398, L58
- Renzini, A., & Daddi, E. 2009, *The Messenger*, 137, 41
- Salpeter, E. E. 1955, *ApJ*, 121, 161
- Santini, P., et al. 2009, *A&A*, 504, 751
- Savaglio, S., et al. 2005, *ApJ*, 635, 260
- Shapiro, K. L., et al. 2009, *ApJ*, 701, 955
- Shi, F., Kong, X., Li, C., & Cheng, F. Z. 2005, *A&A*, 437, 849
- Smail, I., Chapman, S. C., Blain, A. W., & Ivison, R. J. 2004, *ApJ*, 616, 71
- Steidel, C. C., Shapley, A. E., Pettini, M., Adelberger, K. L., Erb, D. K., Reddy, N. A., & Hunt, M. P. 2004, *ApJ*, 604, 534
- Storchi-Bergmann, T., Calzetti, D., & Kinney, A. L. 1994, *ApJ*, 429, 572

- Swinbank, A. M., Smail, I., Chapman, S. C., Blain, A. W., Ivison, R. J., & Keel, W. C. 2004, *ApJ*, 617, 64
- Teplitz, H. I., et al. 2000, *ApJ*, 533, L65
- Tremonti, C. A., et al. 2004, *ApJ*, 613, 898
- van Dokkum, P. G., et al. 2004, *ApJ*, 611, 703
- Vanzella, E., et al. 2005, *A&A*, 434, 53
- Veilleux, S., & Osterbrock, D. E. 1987, *ApJS*, 63, 295
- Ward, M. J., Done, C., Fabian, A. C., Tennant, A. F., & Shafer, R. A. 1988, *ApJ*, 324, 767
- Woosley, S. E., & Weaver, T. A. 1995, *ApJS*, 101, 181
- Yuan, T.-T., & Kewley, L. J. 2009, *ApJ*, 699, L161

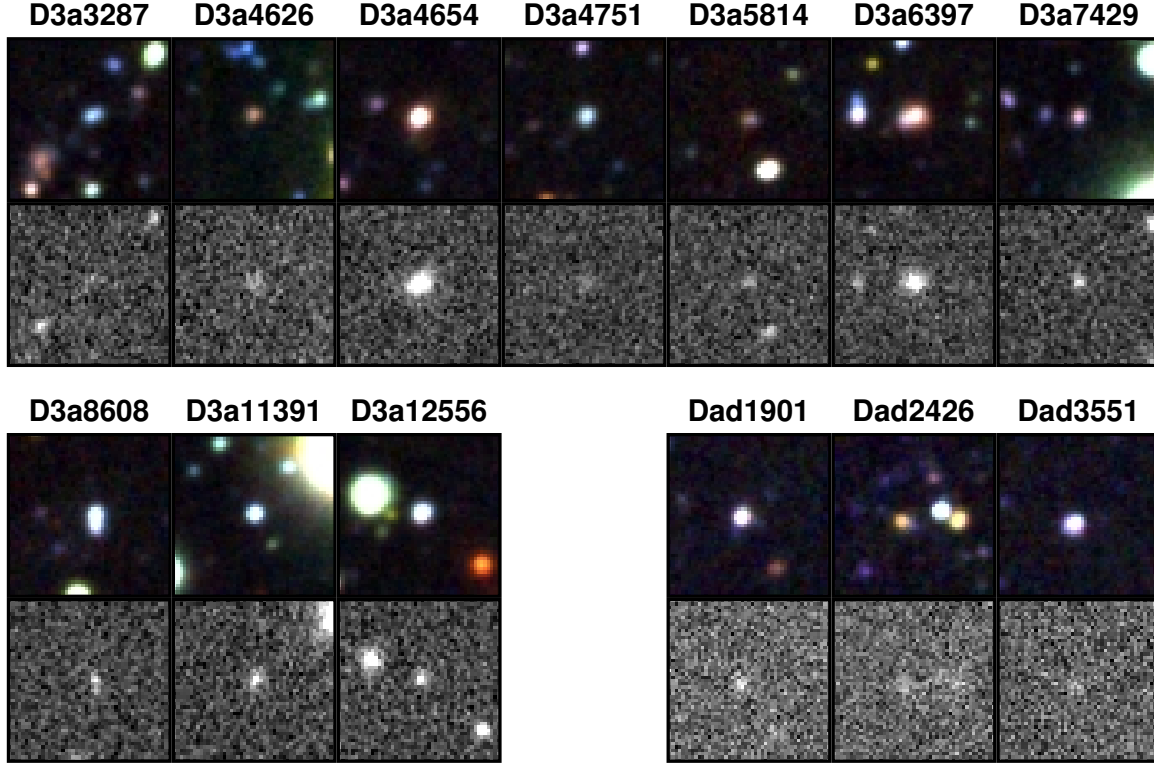


Figure 1. Cutout images ($\simeq 15'' \times 15''$) of *sBzKs* with $H\alpha$ detection in our sample. North is up and east is to the left. Each pair consists of composite color image (top) and *K*-band image (bottom). Composite color images are created with Subaru/Suprime-Cam *BRz'* and *Blz'* for Deep3a and Daddi fields, respectively. Objects are located at the center except for Dad 2426-b which can be seen at 3 arcsec west from Dad 2426.

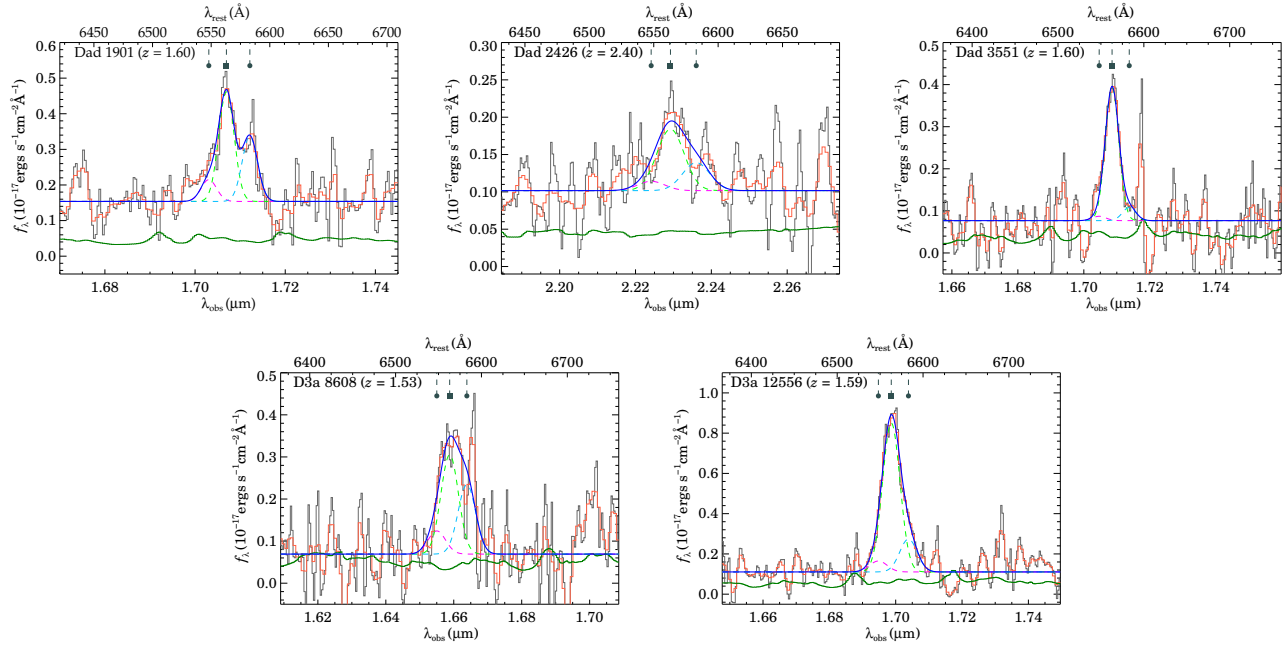


Figure 2. One-dimensional spectra around the $H\alpha$ emission line for the spectra taken with OHS/CISCO. Black, orange, and green lines correspond to raw, 40 \AA boxcar smoothed, and 1σ sky fluctuation spectra, respectively. Gaussian functions fitted to the smoothed spectrum are also shown with dashed lines which respectively correspond to $H\alpha$ (light green), $[\text{N II}]\lambda 6548$ (magenta) and $[\text{N II}]\lambda 6583$ (light blue). The sum of these three Gaussian is shown with blue solid line. Positions of $[\text{N II}]\lambda\lambda 6548, 6583$ and $H\alpha$ are indicated by gray dashed lines with circles and squares, respectively.

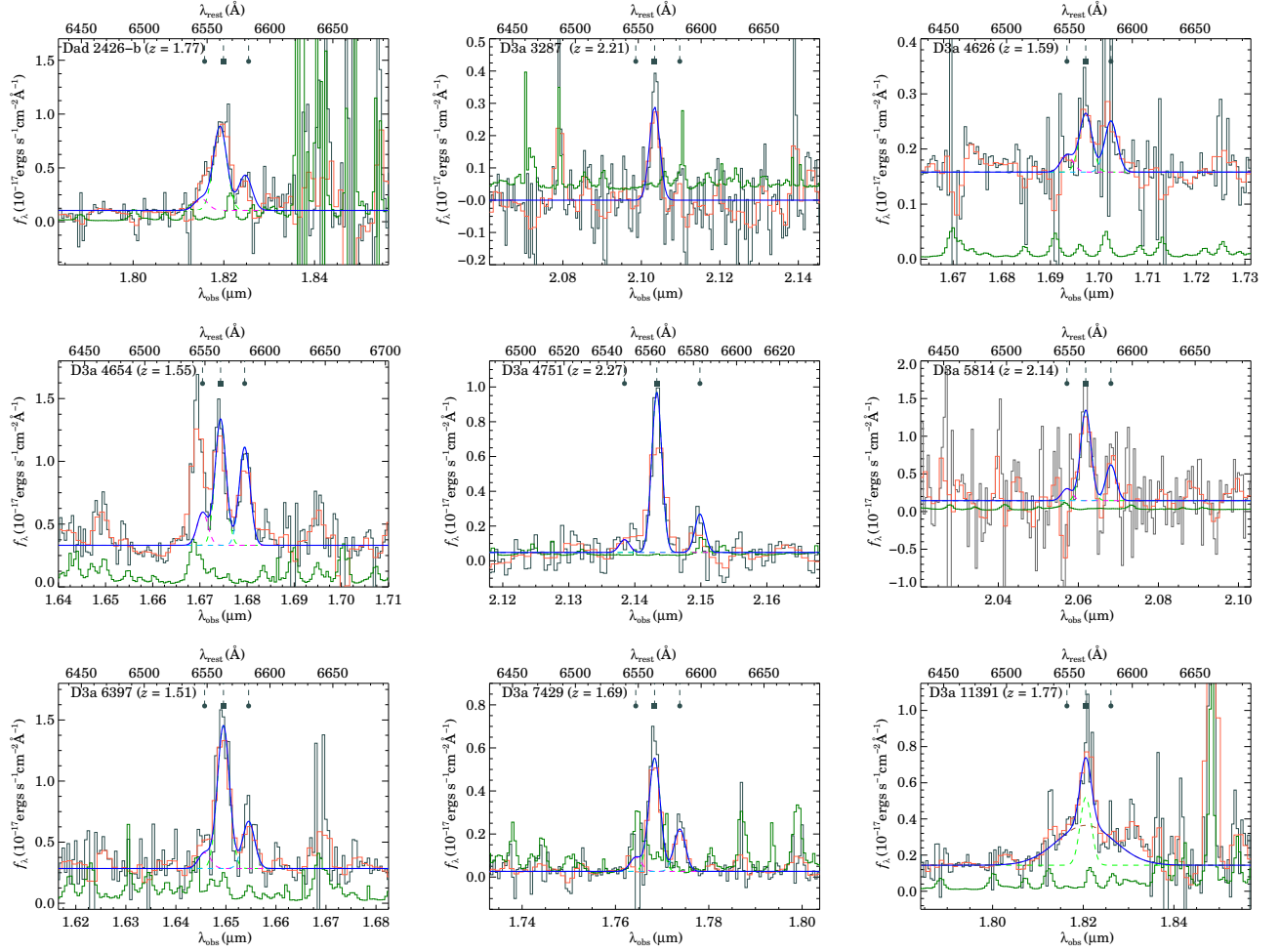


Figure 3. One-dimensional spectra around the $H\alpha$ emission line for the spectra taken with SINFONI. The same line coding as in Figure 2 is used to indicate observed and fitted Gaussian functions. For the D3a-11391 the narrow and broad $H\alpha$ components of the fit are indicated as light green and brown dashed lines, respectively. The positions of $[N II]\lambda\lambda 6548, 6583$ and $H\alpha$ are also indicated by dashed lines with circles and squares, respectively. For the smoothed spectra, a 20 \AA boxcar smoothing kernel was used.

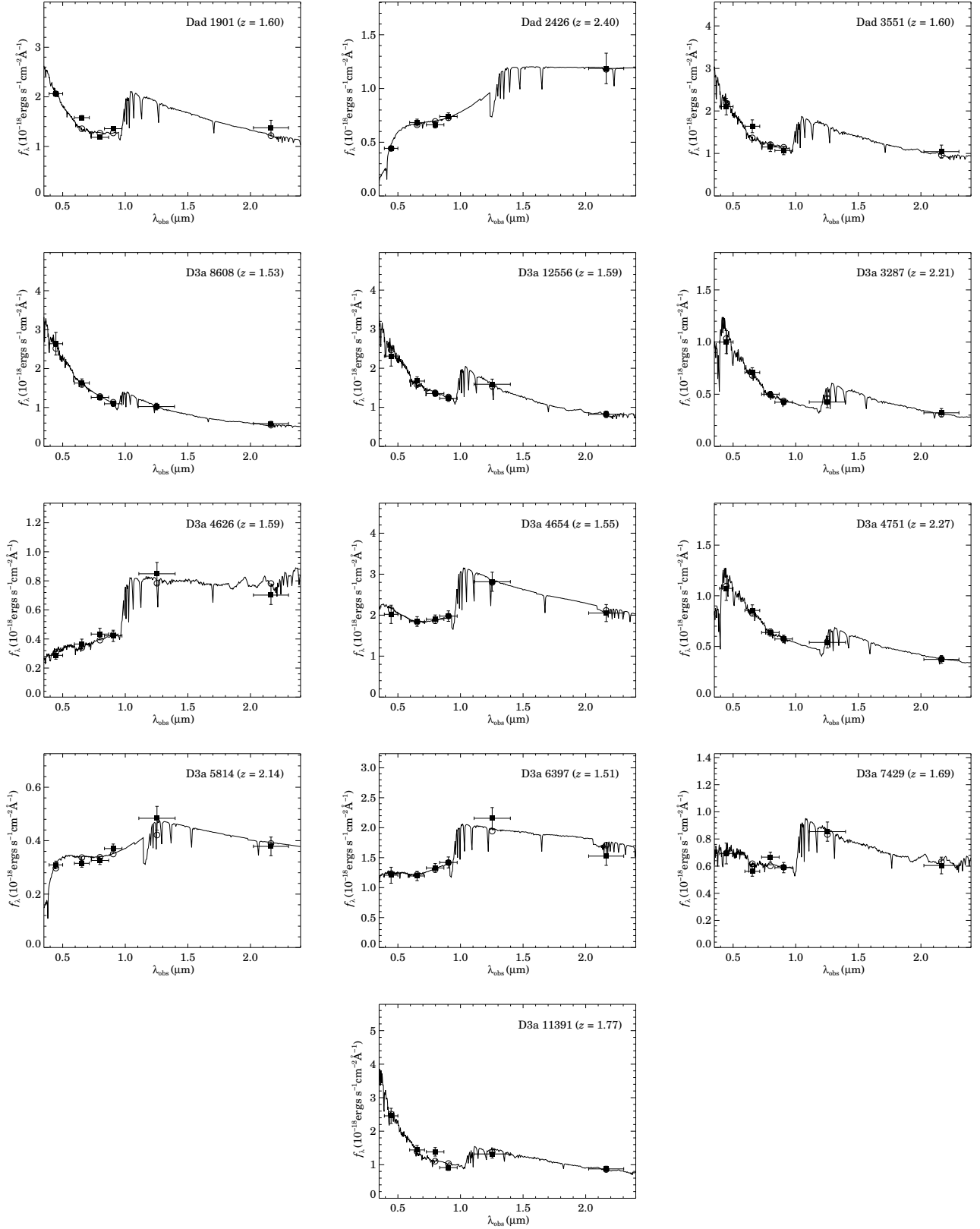


Figure 4. The SEDs of $H\alpha$ detected $sBzKs$: filled squares show the observed flux from broad-band photometry, while solid lines show the best-fit SED from PÉGASE.2 models. Open circles show model magnitudes derived by convolving best-fit SED with the filter response curves. The agreement between the observed and fitted photometry is typically very good and so often the open circles are hidden by the filled circles. Note that Dad 2426-b is excluded here because it is a serendipitous object not in our K -selected catalog.

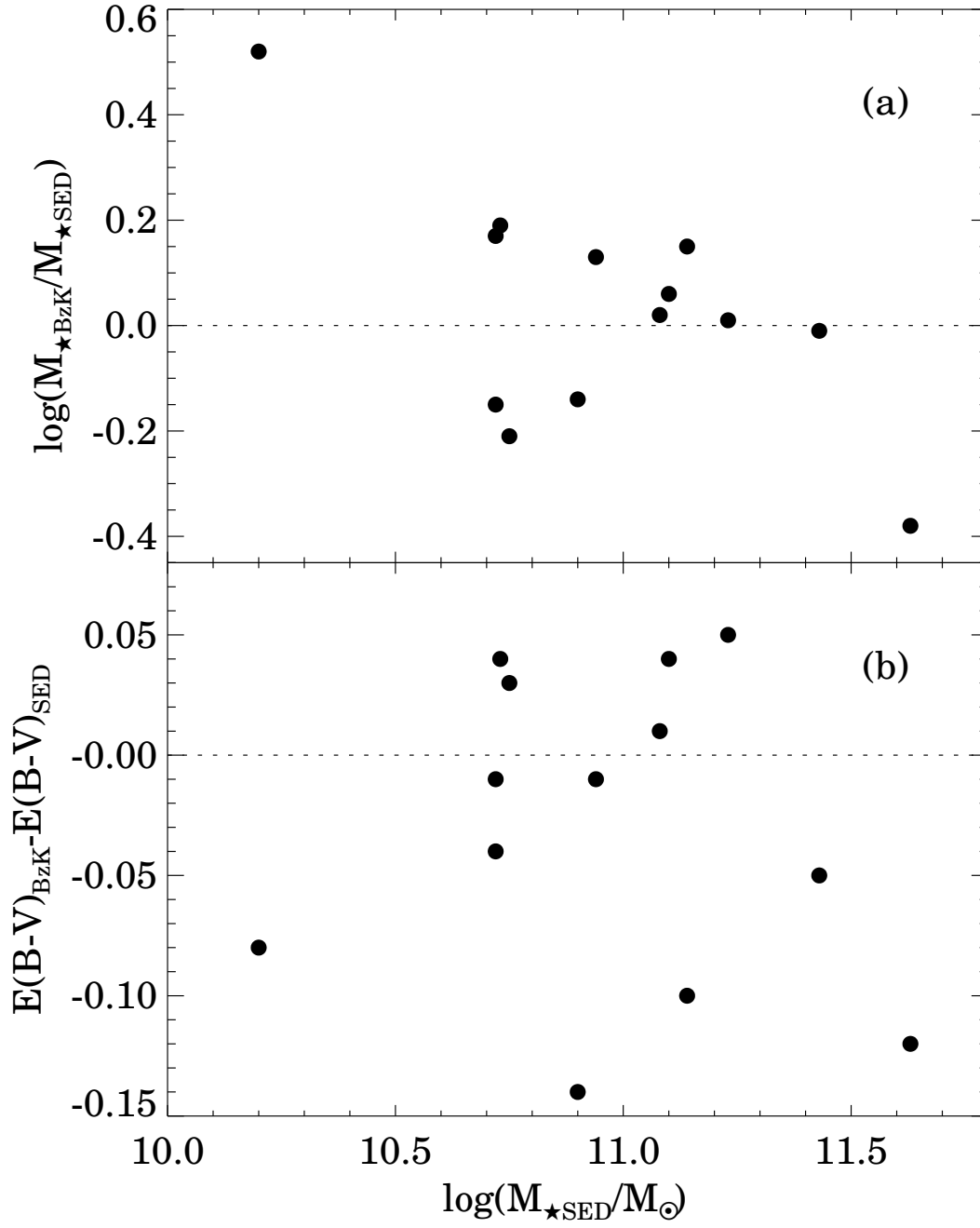


Figure 5. A comparisons of (a) stellar masses and (b) reddenings as derived from *BzK*-based formulae and from SED fitting, as a function of stellar mass from the SED fitting.

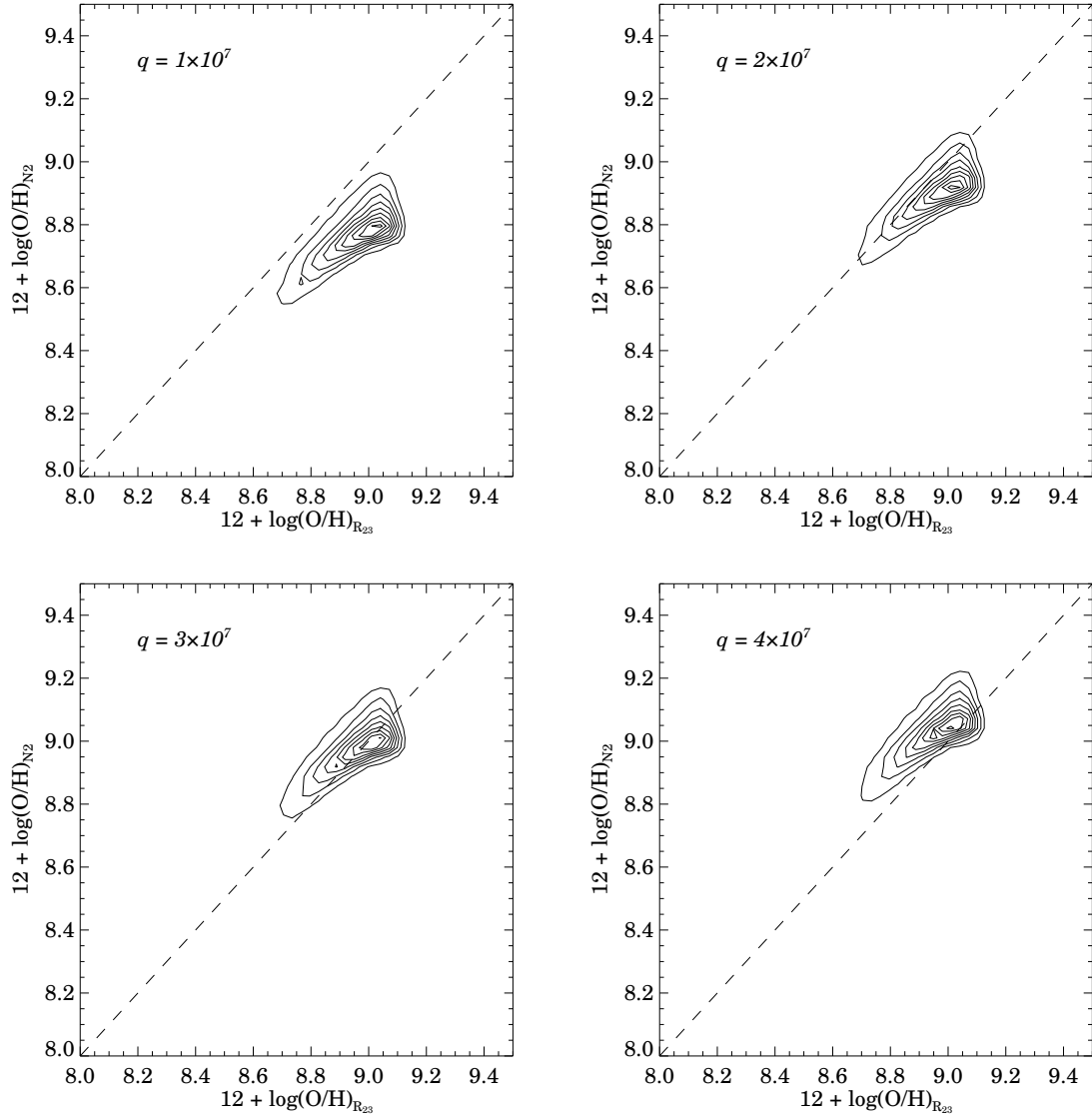


Figure 6. The correlation between the metallicity derived from the R_{23}/O_{32} parameter (Equation 6) and from the N2 indices (Equation 5) for 75,561 star-forming galaxies in the SDSS DR4 release. The various panels refer to different assumed values for the ionization parameter q in the N2 calibration, as indicated. It appears that $q \simeq 3 \times 10^7$ is appropriate for metal-rich galaxies if a constant value is assumed.

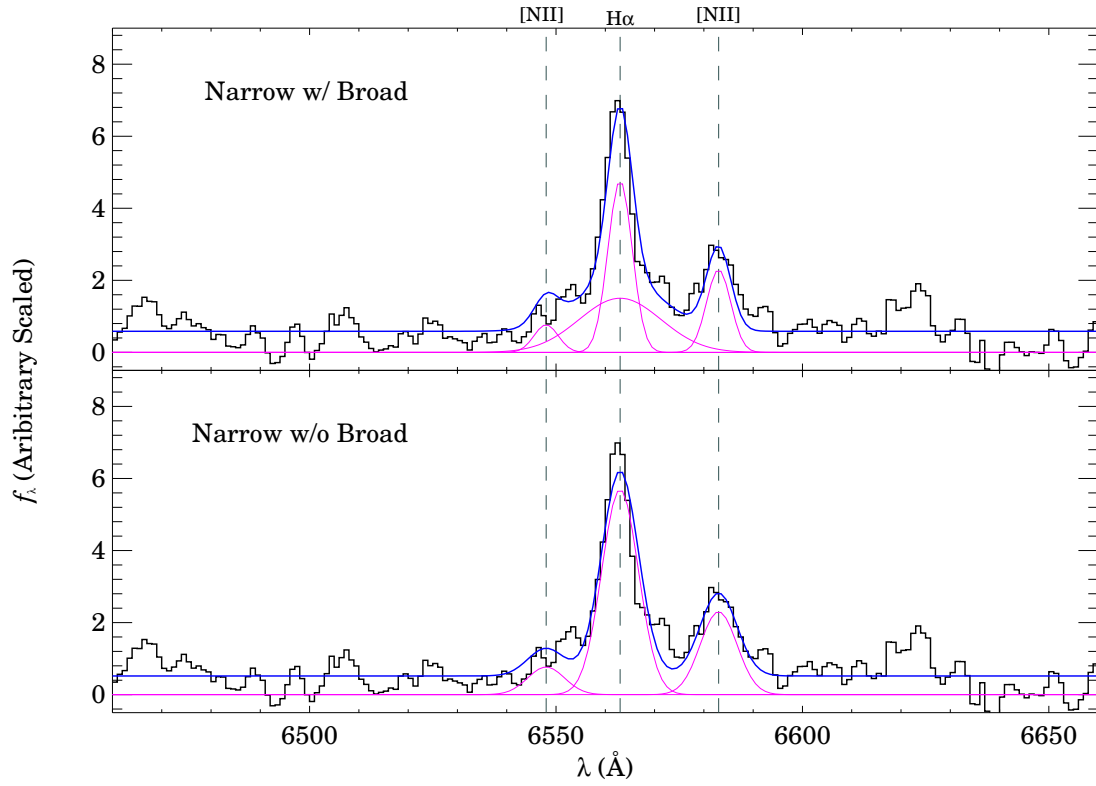


Figure 7. The stacked spectrum of the six SINFONI $H\alpha$ -detected objects (solid black lines). The positions of $H\alpha$ and the two $[N\ II]$ lines are marked at the top of the panel with dashed lines. Best fit multi-Gaussian profiles are shown with solid blue lines for the total spectrum, and with solid magenta lines for its individual components. In the top panel, a broad $H\alpha$ component is included while only the narrow line components are used for the fit in the bottom panel.

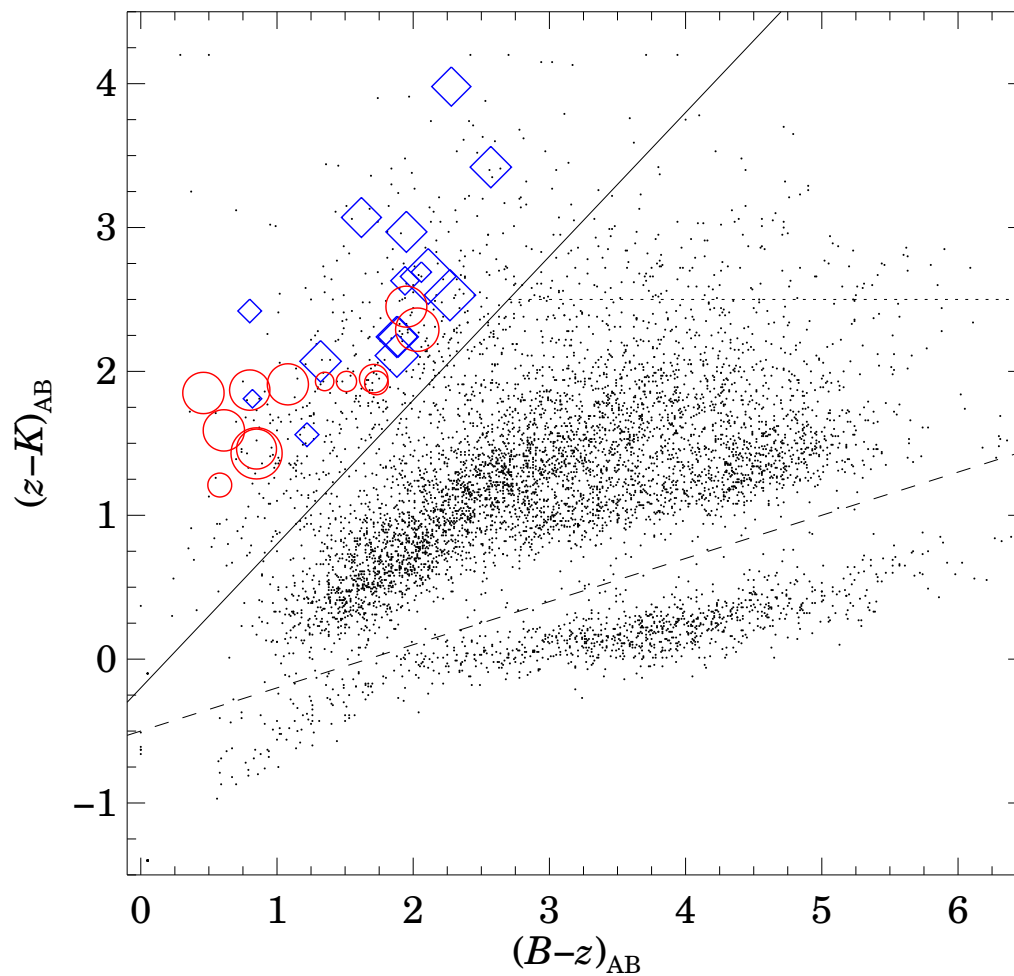


Figure 8. The $(B-z)_{AB}$ vs. $(z-K)_{AB}$ colors of the objects in the Deep3a field and the Daddi field. Black dots show objects in the K -selected catalog, while open circles (red) and open triangles (blue) with sizes proportional to the K -band luminosity show $sBzKs$ in the present study, with and without $H\alpha$ detection, respectively. Solid, dotted, and dashed lines separate $sBzKs$, passive BzK galaxies ($pBzKs$), and stars (below the dashed line) from other populations (see Daddi et al. 2004b; Kong et al. 2006).

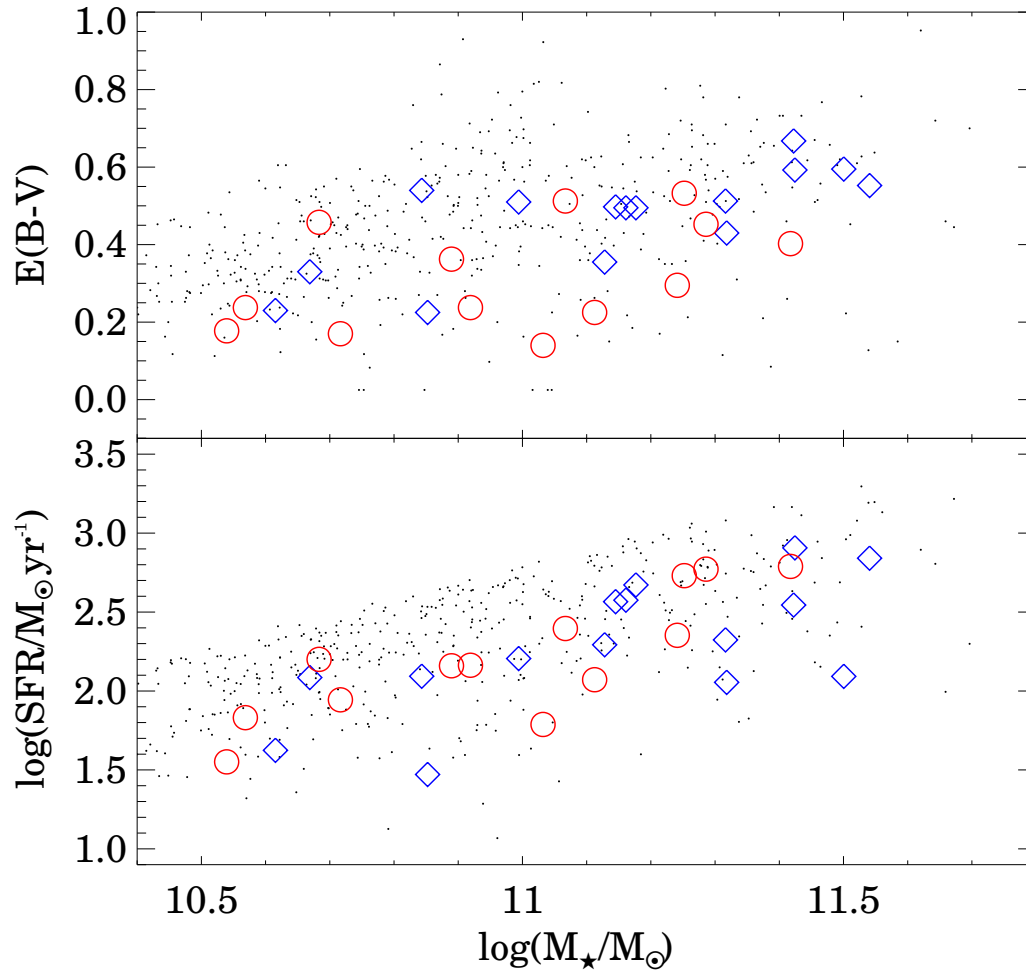


Figure 9. Top: the BzK -based $E(B-V)$ as a function of BzK -based stellar mass. Symbols are as in Figure 8. Bottom: the same as in the top panel, but for the extinction corrected SFR derived from the rest-frame 1500\AA luminosity, with extinction correction based on the $E(B-V)$ values plotted on the top panel.

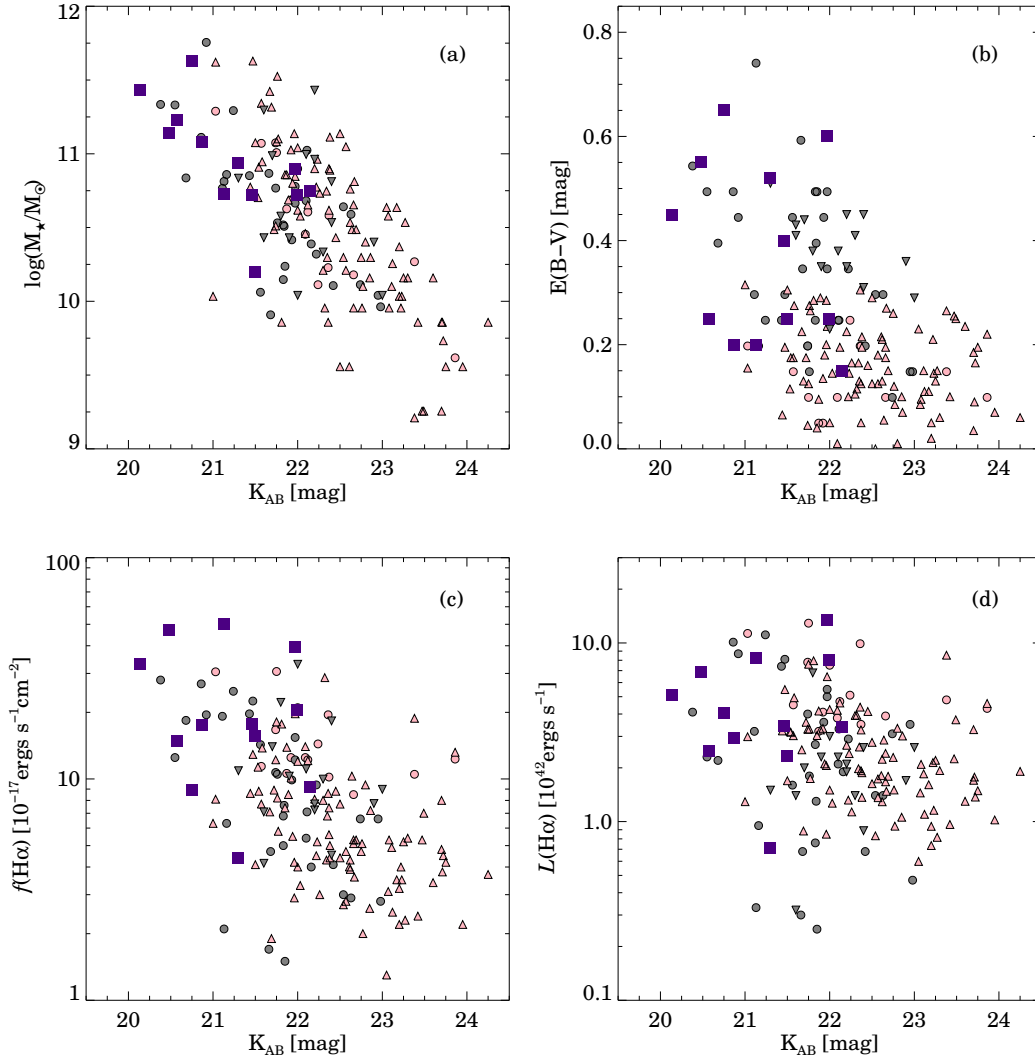


Figure 10. Stellar mass, reddening and $H\alpha$ properties as a function of the K -band magnitude are plotted for the galaxies in the present study and those from other $H\alpha$ surveys. The various panels give: (a) stellar mass, (b) reddening, (c) $H\alpha$ flux, and (d) $H\alpha$ luminosity. Our $sBzK$ sample is shown with filled indigo squares. rest-frame UV-selected BX/BM galaxies from Erb et al. (2006b,c) and rest-frame optically selected $sBzK$ s from Hayashi et al. (2009) are shown with pink triangles and gray upside-down triangles, respectively. Circles represent $z \simeq 2$ star-forming galaxies observed by SINS survey (Förster Schreiber et al. 2009). For SINS galaxies, BX/BM galaxies and rest-frame optically selected galaxies are shown with pink and gray symbols, respectively.

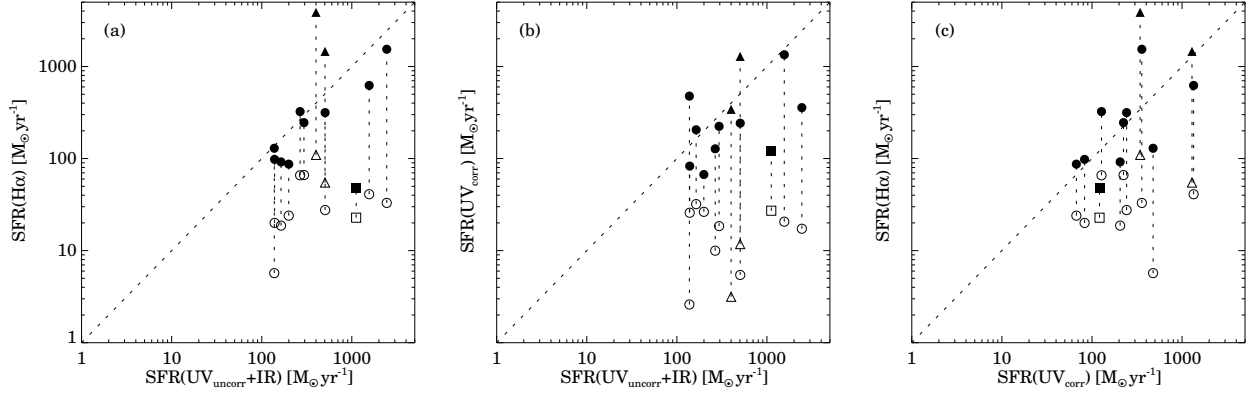


Figure 11. Comparisons of SFRs from different indicators: (a) the SFR from $H\alpha$ vs. the SFR from extinction uncorrected rest-frame UV luminosity and far-infrared luminosity derived from the $24\mu\text{m}$ flux; (b) the SFR from rest-frame UV luminosity vs. SFR (UV+IR); (c) the SFR($H\alpha$) vs. extinction-corrected SFR(UV). In all panels, open and filled symbols refer to SFRs before and after extinction correction, respectively, connected by vertical dotted lines. An object with MIR-excess is shown with square symbol and objects with SFR($H\alpha$) much higher than other estimators are shown as triangles.

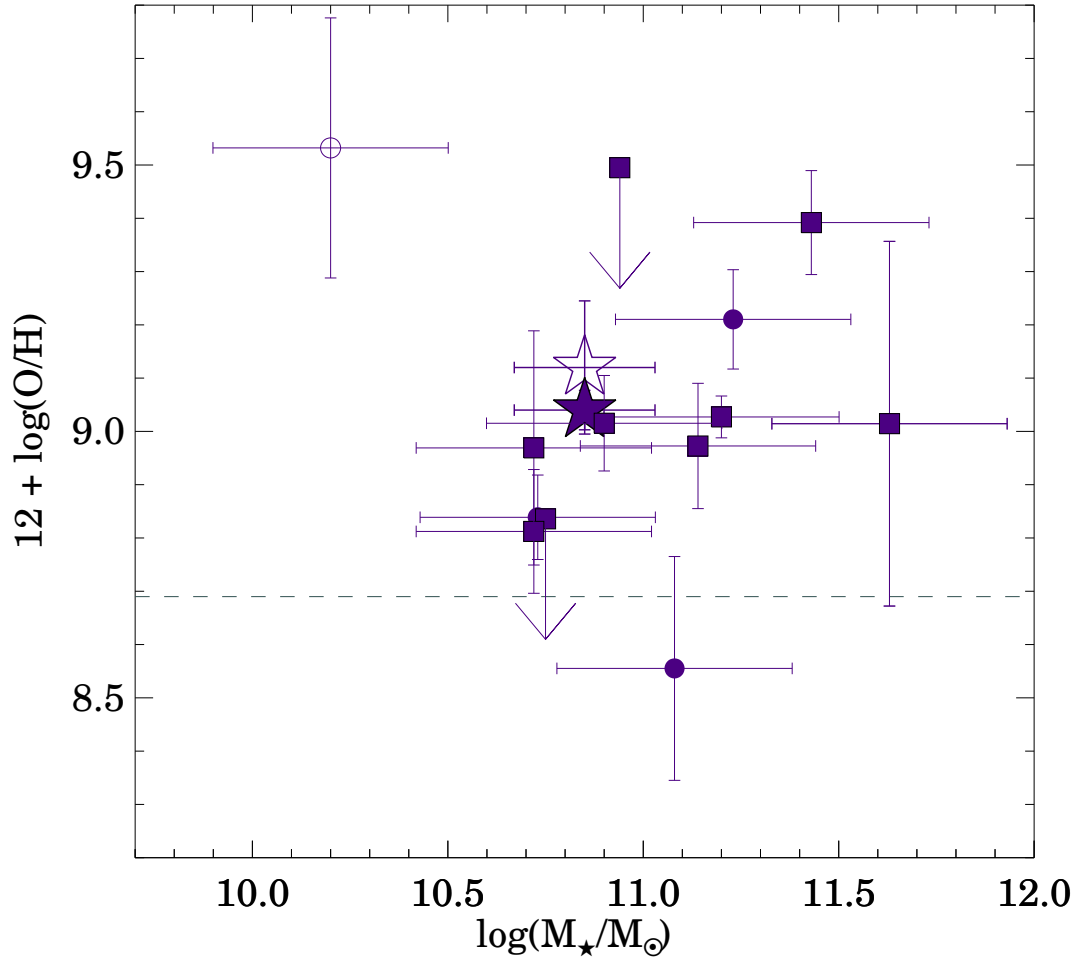


Figure 12. The M_* - Z relation for *sBzKs* at $z \sim 2$. Filled and open circles and squares represent objects with $[\text{N II}]/\text{H}\alpha < 0.7$ and $[\text{N II}]/\text{H}\alpha > 0.7$, respectively. Circles and squares represent metallicities from OHS/CISCO and SINFONI data, respectively. A typical error bar for the stellar mass of 0.3 dex is indicated for each galaxy. Stars represent the values derived from the stacked spectra by means of profile fitting with and without a broad-line $H\alpha$ component (open and filled star, respectively). The horizontal dashed line shows the solar oxygen abundance, $12 + \log(\text{O}/\text{H})_{\odot} = 8.69$ (Allende Prieto et al. 2001).

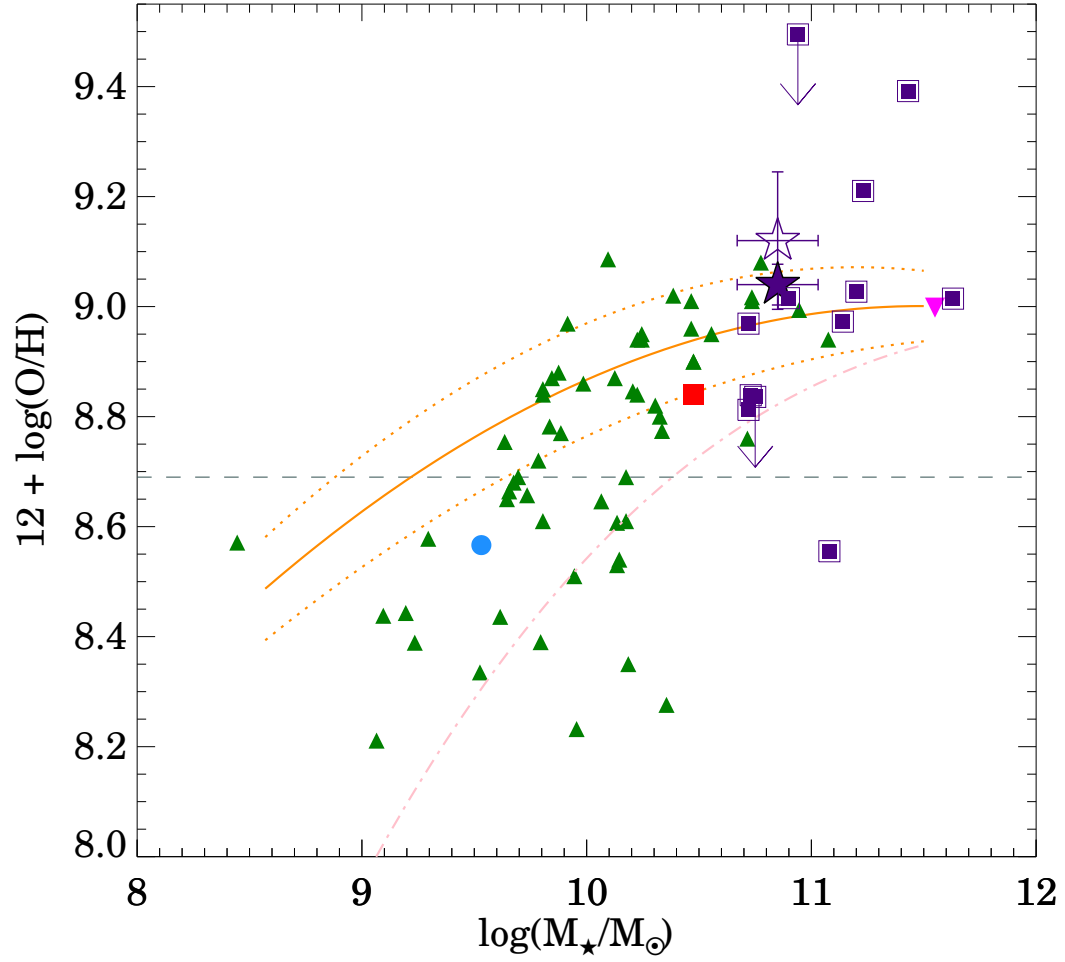


Figure 13. The M_* - Z relations for galaxies at $z = 0.1$, $\simeq 0.7$, and $\simeq 2$ from various samples and sources. Filled indigo squares with border show the non-AGN $sBzK$ s in our sample observed by OHS/CISCO and SINFONI, and filled star and the open stars refer to the stacked spectrum, as in Figure 12. Solid and dotted orange lines show the local M_* - Z relation derived from SDSS data (see text), along with its $\pm 1\sigma$ range. Green filled triangles represent $z \simeq 0.7$ galaxies in GDDS/CFRS sample (Savaglio et al. 2005). A DRG (van Dokkum et al. 2004) is plotted as a magenta upside-down triangle. The mean M_* - Z relation for BX/BM galaxies is shown by the pink dot-dashed line. Cyan circle and red square represent MS 1512-cB58 (Teplitz et al. 2000; Baker et al. 2004) and the median value for the SMGs (Smail et al. 2004; Swinbank et al. 2004), respectively. In this plot error bars are omitted and stellar mass and metallicity are converted to the Salpeter IMF and to the KK04 metallicity calibration, respectively. The horizontal dashed line indicates the solar oxygen abundance.

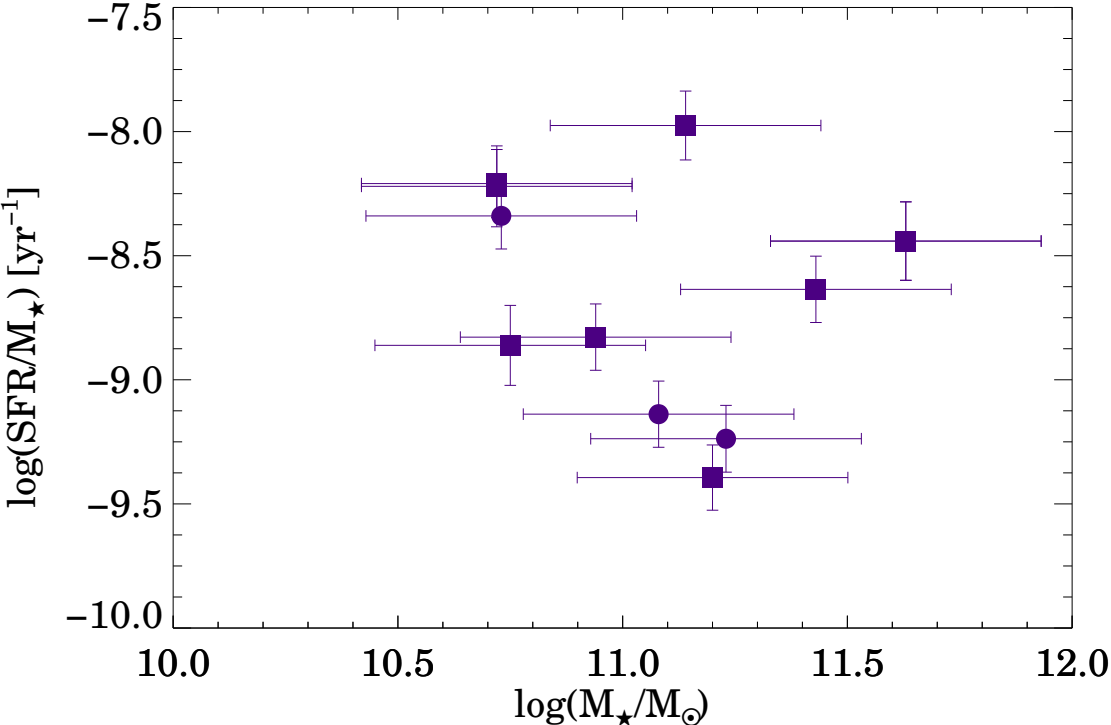


Figure 14. The SSFRs of *sBzKs* in this study are plotted as a function of galaxy stellar mass. Symbols are the same as in Figure 12. A typical mass error of a factor of 2 (0.3 dex) is adopted for all galaxies. The objects possibly dominated by an AGN are not plotted in this figure.

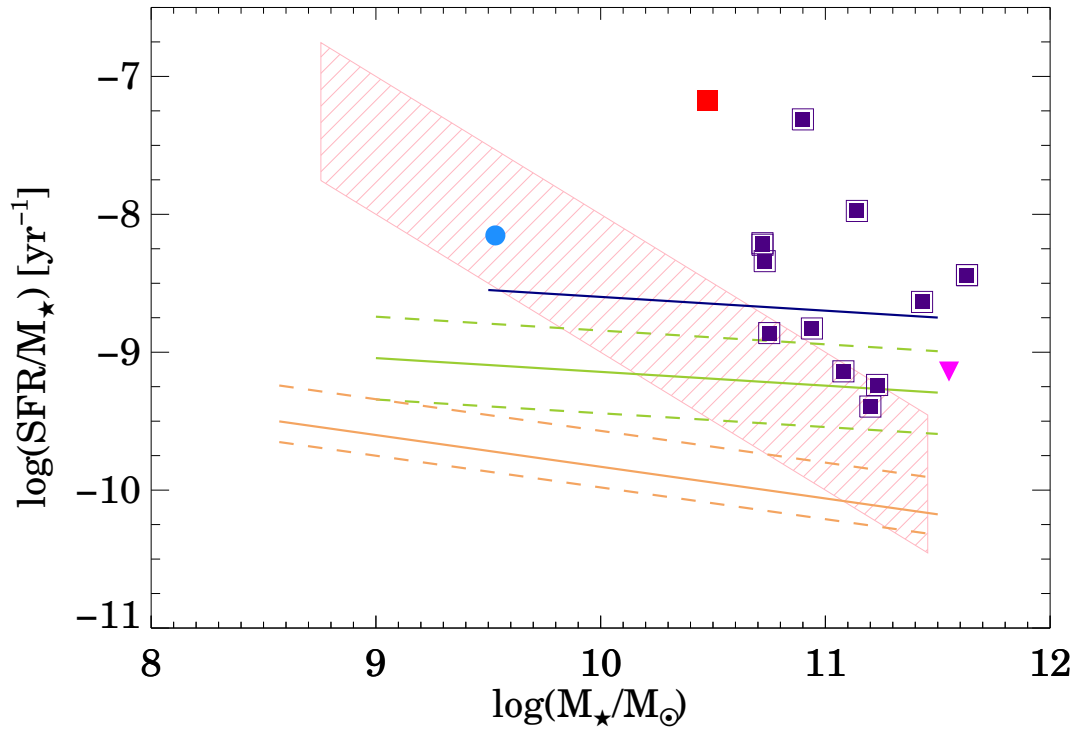


Figure 15. The SSFRs for different galaxy samples are plotted as a function of galaxy stellar mass. Filled indigo squares with border show non-AGN $sBzK$ s in our sample. Magenta square, red upside-down triangle, and cyan circle refer to a DRG (van Dokkum et al. 2004), to the median of SMGs (Smail et al. 2004; Swinbank et al. 2004), and to MS 1512-cB58 (Teplitz et al. 2000; Baker et al. 2004), respectively. The pink hatched band shows the region occupied by UV-selected BX/BM galaxies at $z \simeq 2$ from Erb et al. (2006c). Solid lines represent respectively the fits for the M_* -SSFR relations at $z \simeq 2$ (indigo; Daddi et al. 2007a), and those at $z \simeq 1$ and $z \simeq 0$ (green and orange, respectively; Elbaz et al. 2007). Dotted and dashed lines associated with solid lines represent the 1σ scatter of the distributions.

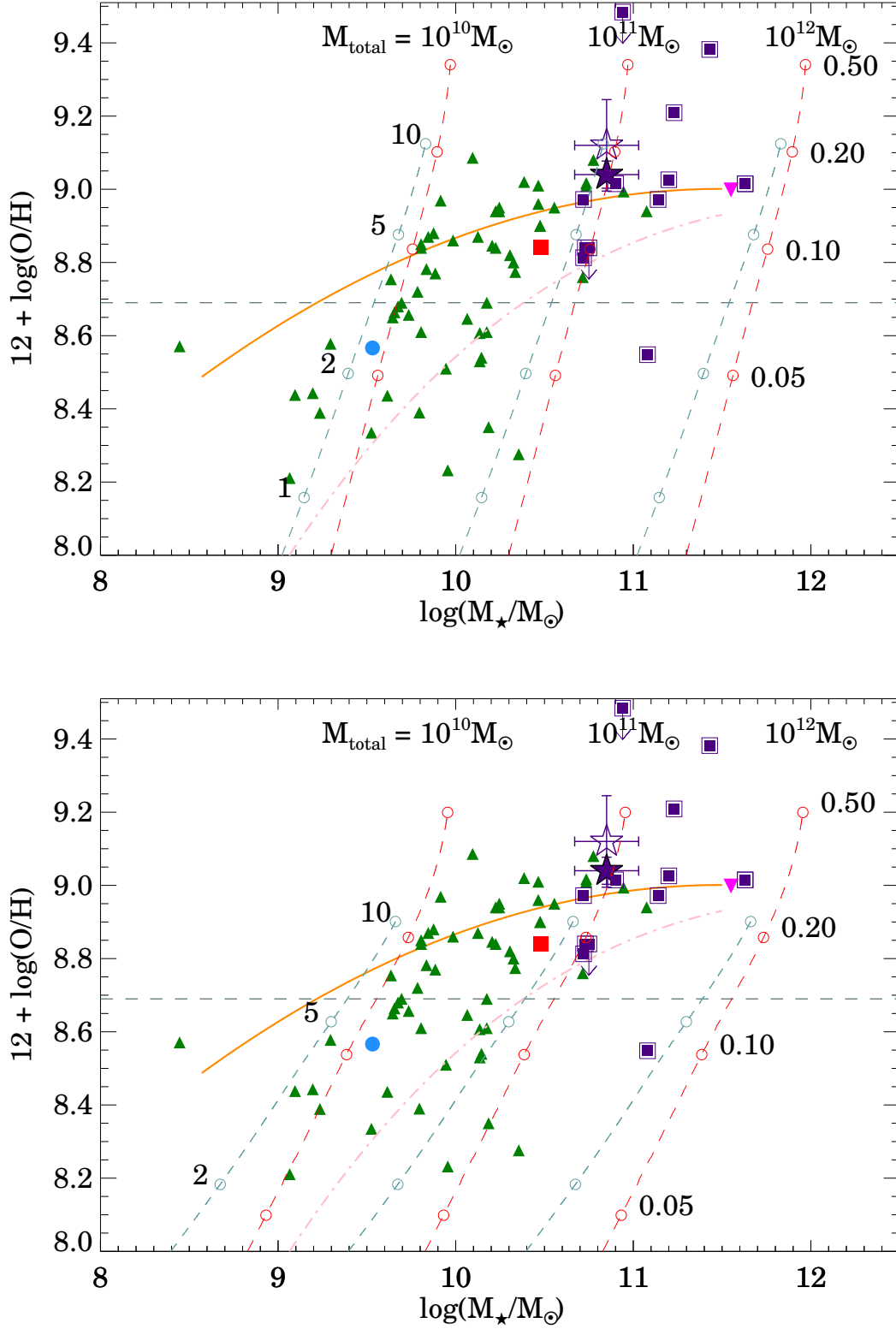


Figure 16. Model tracks from PEGASE.2 overplotted on the M_* - Z relations presented in Figure 13. Top and bottom panels refer to closed-box and infall models, respectively. Red and light-blue dashed lines correspond to $\tau_{\text{sf}} = 0.1$ and 5 Gyr models, respectively. Three parallel lines for each color represent the initial total gas mass as indicated at the top of each panel. The numbers near the small open circles along the tracks indicate galaxy ages in Gyr. The corresponding age for each open circle is the same for the lines with the same color.

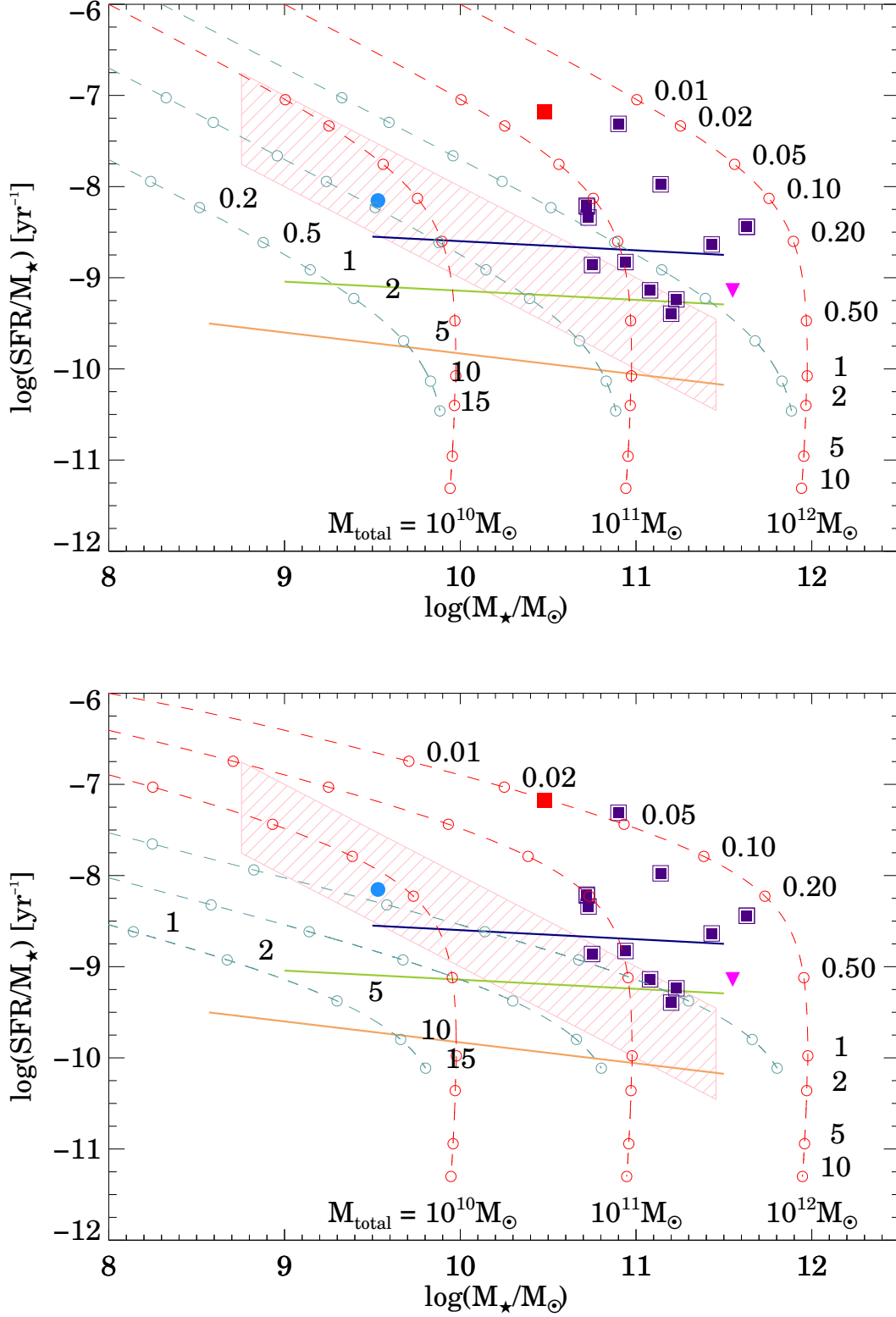


Figure 17. Model tracks from PÉGASE.2 overlotted on Figure 15. Top and bottom panels show tracks from closed-box and infall models, respectively. Red and light-blue dashed lines correspond to $\tau_{\text{sf}} = 0.1$ and 5 Gyr, respectively. Three parallel line sets of each color represent the initial total gas mass of as indicated. Small open circles and texts along the tracks indicate galaxy ages in Gyr. Note that the metallicity with given τ_{sf} and age is independent of M_{total} .

Table 1
Coordinates and Photometric Properties

ID	RA (J2000)	Dec (J2000)	z_{UV}	B (mag)	R (mag)	I (mag)	z' (mag)	J (mag)	Ks (mag)	$B-z'$ (mag)	$z'-Ks$ (mag)	$\log M_*$ ^a ($10^{11} M_\odot$)	$E(B-V)$ ^a (mag)
<i>Hα detection</i>													
D3a 3287	11 24 37.7	-21 49 37.0	2.20	24.35	23.89	23.84	23.74	23.03	22.15	0.61	1.59	10.54	0.18
D3a 4626	11 24 59.1	-21 47 35.8	...	25.70	24.61	23.99	23.75	22.28	21.30	1.95	2.45	11.07	0.51
D3a 4654	11 24 53.3	-21 47 36.7	...	23.58	22.85	22.39	22.07	20.98	20.14	1.51	1.93	11.42	0.40
D3a 4751	11 24 50.0	-21 47 23.1	2.26	24.27	23.69	23.57	23.42	22.77	21.99	0.85	1.43	10.57	0.24
D3a 5814	11 24 34.4	-21 45 49.4	2.14	25.62	24.77	24.30	23.89	22.89	21.97	1.73	1.92	10.76	0.46
D3a 6397	11 25 10.5	-21 45 06.1	2.00	24.14	23.32	22.78	22.43	21.27	20.48	1.71	1.95	11.29	0.45
D3a 7429	11 25 12.9	-21 43 30.1	...	24.74	24.14	23.52	23.39	22.27	21.46	1.35	1.93	10.89	0.36
D3a 8608	11 25 06.3	-21 41 52.7	1.53	23.29	22.99	22.83	22.71	22.09	21.50	0.58	1.21	10.72	0.17
D3a 11391	11 24 54.7	-21 34 13.3	...	23.37	23.12	22.73	22.91	21.80	21.06	0.46	1.85	11.16	0.14
D3a 12556	11 25 11.6	-21 35 48.6	1.58	23.44	22.96	22.76	22.59	21.60	21.13	0.85	1.46	10.92	0.24
Dad 1901	14 49 41.4	8 59 50.5	1.60	23.56	23.02	22.90	22.48	...	20.57	1.08	1.91	11.24	0.30
Dad 2426	14 49 29.0	8 51 52.9	2.36	25.07	23.92	23.56	23.04	...	20.75	2.03	2.29	11.25	0.53
Dad 2426-b ^b
Dad 3551	14 48 59.6	8 52 06.6	1.60	23.54	22.98	22.93	22.74	...	20.87	0.80	1.87	11.10	0.21
<i>Hα non-detection</i>													
D3a 6004	11 25 03.8	-21 45 32.7	2.39	25.88	24.69	24.31	23.93	22.79	20.96	1.95	2.97	11.32	0.51
D3a 6048	11 25 23.1	-21 45 32.2	1.41	24.33	23.88	23.28	23.01	21.99	20.94	1.32	2.07	11.13	0.36
D3a 7182	11 25 12.4	-21 43 48.1	...	26.74	24.68	23.41	21.99	2.06	2.69	10.84	0.54
D3a 8249	11 25 15.9	-21 42 23.3	2.06	25.25	24.38	23.47	22.98	21.54	20.45	2.27	2.53	11.42	0.59
D3a 12153 ^c	11 24 40.7	-21 36 19.2	2.34	25.04	24.58	24.29	24.24	...	21.82	0.80	2.42	10.85	0.23
D3a 13557	11 25 04.9	-21 37 09.1	2.40	26.15	25.30	24.53	24.21	22.75	21.58	1.94	2.63	10.99	0.51
D3a 13600	11 25 05.9	-21 37 13.1	2.27	24.71	24.28	24.02	23.89	22.78	22.08	0.82	1.81	10.62	0.23
D3a 14009 ^c	11 24 34.4	-21 38 34.1	2.43	24.59	23.65	23.56	23.37	...	21.81	1.22	1.56	10.67	0.33
Dad 759	14 50 11.4	9 07 51.3	...	26.93	25.21	25.16	24.36	...	20.94	2.57	3.42	11.42	0.67
Dad 1250	14 49 59.2	8 56 18.0	...	25.70	24.88	24.54	24.08	...	21.01	1.62	3.07	11.32	0.43
Dad 2079	14 49 37.3	8 58 16.6	0.73 ^d	25.07	24.12	23.45	23.19	...	20.95	1.88	2.24	11.16	0.50
Dad 2742	14 49 20.5	8 50 52.4	2.12	24.83	24.02	23.67	22.95	...	20.84	1.88	2.11	11.18	0.50
Dad 3882	14 48 49.0	8 53 15.1	2.25	25.12	24.01	23.76	23.23	...	20.99	1.89	2.24	11.15	0.50
Dad 3977	14 48 45.8	8 57 45.8	...	25.00	23.85	23.50	22.89	...	20.23	2.11	2.66	11.54	0.55
Dad 4008	14 48 44.9	8 53 46.9	2.22	27.31	25.97	25.84	25.03	...	21.05	2.28	3.98	11.50	0.59

Note. — All magnitudes are shown in the AB system and are measured within a $2''$ aperture (K06).

^a Derived from the BzK -calibration of Daddi et al. (2004a). See Equations (1) and (2) in §4.1.

^b This object is not included in our K -selected catalog, but it was serendipitously found in the FoV of SINFONI.

^c This object is not included in our current K -selected catalog. Quoted values are from an older version of the catalog.

^d This object was considered at $z \simeq 2$ based on its photometric redshift, but it was later spectroscopically confirmed to be at $z = 0.73$.

Table 2
Observational Information

ID	Date	Instrument	Grism	Exposure (seconds)
<i>Hα detection</i>				
D3a 3287	2005 April 15	SINFONI	<i>H + K</i>	3600
D3a 4624	2005 April 16	SINFONI ^a	<i>H + K</i>	3600
D3a 4654	2005 April 16	SINFONI	<i>H + K</i>	3600
D3a 4751	2005 April 16	SINFONI	<i>H + K</i>	3600
D3a 5814	2005 April 14	SINFONI	<i>H + K</i>	5400
D3a 6397	2005 April 15	SINFONI	<i>H + K</i>	3600
D3a 7429	2005 April 15	SINFONI	<i>H + K</i>	3600
D3a 8608	2005 April 25	OHS	<i>JH</i>	8400
D3a 11391	2005 April 16	SINFONI ^a	<i>H + K</i>	1800
D3a 12556	2005 April 25	OHS	<i>JH</i>	3600 ^b
	2005 April 26	OHS	<i>JH</i>	3600
Dad 1901	2004 May 1	OHS	<i>JH</i>	8000
Dad 2426	2004 May 6	CISCO	<i>wK</i>	6000
	2005 April 14	SINFONI	<i>H + K</i>	7200
Dad 3551	2005 April 24	OHS	<i>JH</i>	14400
	2005 April 26	OHS	<i>JH</i>	7200 ^c
<i>Hα non-detection</i>				
D3a 6004	2005 April 16	SINFONI	<i>H + K</i>	3600
D3a 6048	2005 April 24	OHS	<i>JH</i>	10800
D3a 7182	2005 April 16	SINFONI	<i>H + K</i> ^a	3600
D3a 8249	2005 April 16	SINFONI	<i>H + K</i>	3600
D3a 12153	2005 April 14	SINFONI	<i>H + K</i>	3600
D3a 13557 ^d	2004 May 6	CISCO	<i>wK</i>	7000
	2005 April 30	CISCO	<i>wK</i>	7000
D3a 13600 ^d	2004 May 6	CISCO	<i>wK</i>	7000
D3a 14009	2005 April 30	CISCO	<i>wK</i>	5000
Dad 759	2005 April 16	SINFONI	<i>H + K</i> ^a	1800
Dad 1250	2005 April 16	SINFONI	<i>H + K</i> ^a	1800
Dad 2079	2004 May 6	CISCO	<i>wK</i>	3000
Dad 2742	2005 April 15	SINFONI	<i>H + K</i>	7200
Dad 3882	2005 April 16	SINFONI	<i>H + K</i>	1800
Dad 3977	2005 April 25	OHS	<i>JH</i>	2400
Dad 4008	2005 April 25	OHS	<i>JH</i>	3600

^a AO-module was used.

^b This exposure was not used because it does not improve S/N ratio due to worse seeing.

^c This exposure was not used because it does not improve S/N ratio due to reduced signal by cloud passage.

^d D3a 13557 and D3a 13600 were supposed to be in the same slit, but the objects were not correctly placed.

^e The target acquisition was failed and the object was not correctly placed in the slit.

Table 3
Emission Line Properties of $H\alpha$ and $[N\text{ II}]\lambda 6583$

ID	$z_{H\alpha}$	$f(H\alpha)$ (10^{-17} ergs s^{-1} cm^{-2})	$EW_{rest}(H\alpha)^{a,b}$ (\AA)	$f([N\text{ II}])$ (10^{-17} ergs s^{-1} cm^{-2})	$EW_{rest}([N\text{ II}])^d$ (\AA)	$[N\text{ II}]/H\alpha$	σ^c km s^{-1}
OHS							
Dad 1901	1.600	15 ± 1	38 ± 8	7.9 ± 0.7	20 ± 4	0.53 ± 0.06	...
Dad 3551	1.603	17 ± 1	55 ± 12	1.6 ± 0.9	5 ± 3	0.09 ± 0.05	...
<i>D3a 8608</i>	1.528	16 ± 2	86 ± 20	11 ± 1	60 ± 13	0.70 ± 0.11	...
D3a 12556	1.588	50 ± 3	184 ± 38	11 ± 3	40 ± 14	0.22 ± 0.06	...
CISCO							
Dad 2426	2.397	9.0 ± 1.8	22 ± 6	3.4 ± 2.7	9 ± 7	0.38 ± 0.31	...
SINFONI							
Dad 2426-b	1.772	31 ± 1	> 194	12 ± 1	> 76	0.39 ± 0.04	245
D3a 3287	2.205	9.2 ± 2.0	89 ± 26	< 2.0	< 19	< 0.22	118
D3a 4626	1.586	4.4 ± 0.3	22 ± 6	< 3.0	< 15	< 0.68	212
D3a 4654	1.551	33 ± 2	52 ± 11	21 ± 1	33 ± 7	0.63 ± 0.05	170
D3a 4751	2.266	21 ± 2	165 ± 37	4.1 ± 1.6	33 ± 14	0.20 ± 0.08	74: ^d
D3a 5814	2.141	39 ± 3	316 ± 68	15 ± 3	120 ± 34	0.38 ± 0.08	169
D3a 6397	1.513	47 ± 5	99 ± 23	16 ± 5	34 ± 13	0.34 ± 0.11	265
D3a 7429	1.694	17 ± 4	96 ± 29	6.0 ± 3.5	32 ± 20	0.34 ± 0.21	125
<i>D3a 11391</i> narrow	1.774	13 ± 1	46 ± 10	187
broad	...	35 ± 2	123 ± 26	1040

Note. — $[N\text{ II}]$ stands for $[N\text{ II}]\lambda 6583$. The object IDs with slanted fonts are considered to be AGN-dominated *sBzKs* judged from a large $[N\text{ II}]/H\alpha$ ratio (D3a-8608) or a broad-line component (D3a-11391).

^a Equivalent widths are calculated by assuming the continuum flux from the best-fit SED. For Dad-2426-b, $K_{AB} = 21.5$ (K06) is used for upper limit of the continuum

^b $H\alpha$ equivalent widths are corrected for underlying stellar $H\alpha$ absorption calculated from the best-fit SED. For Dad-2426-b, the average of the $H\alpha$ absorption line equivalent widths of the other objects, 4.4 \AA , is assumed.

^c The velocity dispersions are corrected for the instrumental resolution, $\sigma_{\text{instrument}} = 85 \text{ km s}^{-1}$.

^d This is smaller than instrumental resolution, hence the uncertainty is large.

Table 4
SED Fitting Results

ID	$E(B-V)_{\text{SED}}^{\text{a,b}}$ (mag)	$\log(M_{\star\text{SED}}/M_{\odot})^{\text{b}}$
OHS		
Dad 1901	0.25	11.23
Dad 3551	0.20	11.08
D3a 8608	0.25	10.20
D3a 12556	0.20	10.73
CISCO		
Dad 2426	0.65	11.63
SINFONI		
Dad 2426-b
D3a 3287	0.15	10.75
D3a 4626	0.52	10.94
D3a 4654	0.45	11.43
D3a 4751	0.25	10.72
D3a 5814	0.60	10.90
D3a 6397	0.55	11.14
D3a 7429	0.40	10.72
D3a 11391	0.10	11.10

^a $E(B-V)$ from the stellar continuum.

^b Derived by SED fitting.

Table 5
Extinctions and $\text{H}\alpha$ Star-formation Rates

ID	A_V^* (mag)	A_V^{gas} (mag)	$A_{\text{H}\alpha}$ (mag)	$L_{\text{H}\alpha}^{\text{a}}$ (10^{42} ergs s^{-1})	$\text{SFR}_{\text{raw}}^{\text{a}}$ ($M_{\odot} \text{ yr}^{-1}$)	$\text{SFR}_{\text{corr}}^{\text{b}}$ ($M_{\odot} \text{ yr}^{-1}$)
OHS						
Dad 1901	1.0	2.1	1.7	2.2 ± 0.2	20 ± 1	98 ± 7
Dad 3551	0.6	1.4	1.1	2.7 ± 0.2	24 ± 1	87 ± 5
D3a 8608	1.0	2.1	1.7	2.2 ± 0.2	19 ± 2	92 ± 12
D3a 12556	0.8	1.7	1.4	8.1 ± 0.6	66 ± 4	246 ± 15
CISCO						
Dad 2426	2.6	5.1	4.2	3.3 ± 0.8	33 ± 7	1540 ± 320
SINFONI						
Dad 2426-b	6.1 ± 0.1	53 ± 2	...
D3a 3287	0.6	1.4	1.1	3.2 ± 0.7	28 ± 6	77 ± 17
D3a 4626	2.1	4.1	3.4	0.6 ± 0.3	5.7 ± 0.4	129 ± 8
D3a 4654	1.8	3.6	3.0	4.6 ± 0.3	41 ± 3	622 ± 39
D3a 4751	1.0	2.1	1.7	7.9 ± 0.6	66 ± 6	323 ± 31
D3a 5814	2.4	4.7	3.9	13 ± 1.0	110 ± 8	3880 ± 290
D3a 6397	2.2	4.3	3.6	6.5 ± 0.7	55 ± 6	1460 ± 160
D3a 7429	1.6	3.2	2.6	3.3 ± 0.7	28 ± 6	315 ± 71
D3a 11391 ^c	0.4	1.0	0.8	2.5 ± 0.3	23 ± 2	48 ± 4

^a Values not corrected for extinction.

^b Extinction corrected values.

^c Only the contribution from the narrow-line component is listed and the narrow-line is assumed to come from star-forming regions.

Table 6
Gas-phase oxygen
abundances

ID	$12 + \log(\text{O}/\text{H})$
OHS	
Dad 1901	9.21 ± 0.09
Dad 3551	8.55 ± 0.21
D3a 8608	(9.53 ± 0.24)
D3a 12556	8.84 ± 0.08
CISCO	
Dad 2426	9.02 ± 0.34
SINFONI	
Dad 2426-b	9.03 ± 0.04
D3a 3287	< 8.84
D3a 4626	< 9.48
D3a 4654	9.38 ± 0.10
D3a 4751	8.81 ± 0.12
D3a 5814	9.02 ± 0.09
D3a 6397	8.97 ± 0.12
D3a 7429	8.97 ± 0.22
D3a 11391	...

Note. — D3a 8608 which has $[\text{N II}]/\text{H}\alpha \geq 0.7$ is considered to host an AGN. Thus the derived metallicity is listed within parentheses.

Table 7
Dynamical masses for
SINFONI objects

ID	$\log(M_{\text{dyn}}/M_{\odot})$
Dad 2426-b	11.6
D3a 3287	11.1
D3a 4626	11.5
D3a 4654	11.3
D3a 4751	10.6
D3a 5814	11.4
D3a 6397	11.7
D3a 7429	11.0
D3a 11391	11.4 ^a

^a Calculated from the velocity dispersion of the narrow-line component.